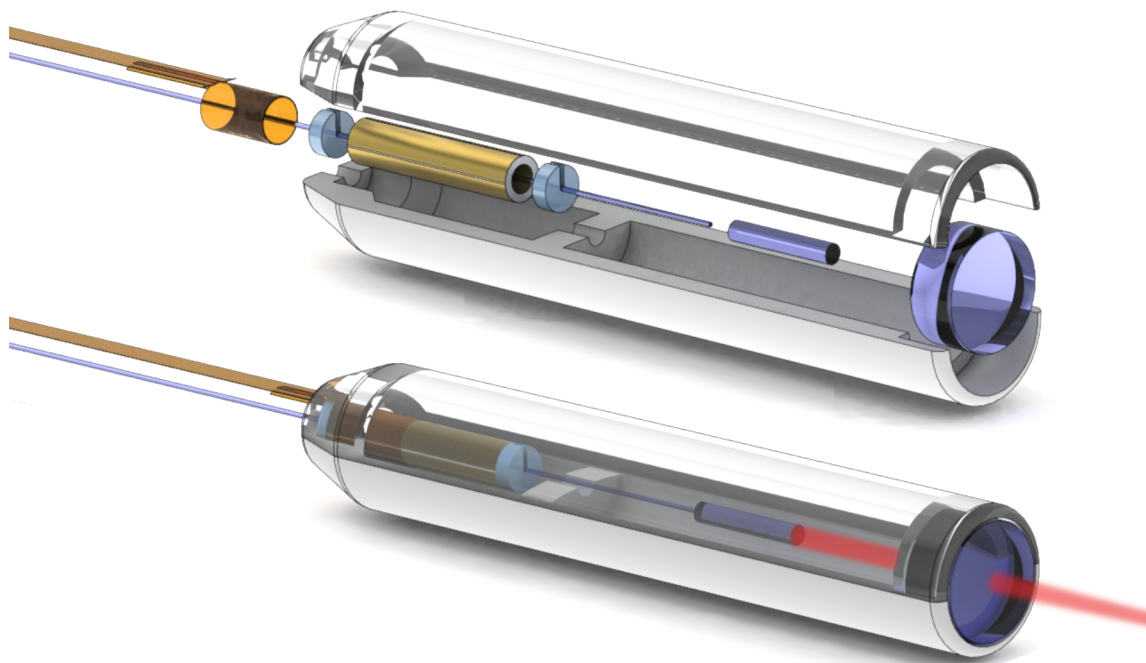


Master's Thesis

Compact OCT scanner for a bimodal endoscopic probe



Sergio Vilches

A master's thesis submitted in partial fulfillment of the requirements for the degree of

Master of Science of Microsystems Engineering

according to the examination regulations at the University of Freiburg for the Master's degree in Microsystems Engineering of July 20, 2009.

Gisela and Erwin Sick Chair of Micro-optics.
Department of Microsystems Engineering (IMTEK)
University of Freiburg
Freiburg im Breisgau, Germany

Author Sergio Vilches

Thesis period April 1, 2016 to February 23, 2017

Referees Prof. Dr. Hans Zappe, Gisela and Erwin Sick Chair of Micro-optics
Prof. Dr. Alexander Rohrbach, Bio- and Nano-Photonics research group

Supervisor M.Sc. Simon Kretschmer, Gisela and Erwin Sick Chair of Micro-optics

Title page **Top:** Exploded view of the single modality OCT demonstrator probe. **Bottom:** Render of the assembled probe, showing the optical beampath.

Declaration according to the Examination Regulations:

I hereby confirm to have written the following thesis on my own, not having used any other sources or resources than those listed. All passages taken over literally or correspondingly from published sources have been marked accordingly. Additionally, this thesis has not been prepared or submitted for another examination, neither partially nor completely.

Freiburg, February 23, 2017

Sergio Vilches

Zusammenfassung

Endoskopische Untersuchungstechniken spielen in der modernen Medizin eine zunehmend wichtigere Rolle. Das Ziel der Endoskopie ist dabei möglichst umfangreich Informationen für eine verlässliche Diagnose zu sammeln. Durch die Kombination verschiedener optischer Abbildungstechniken in einem Endoskop wird aktuell versucht die Möglichkeiten der endoskopbasierten Diagnostik zu erweitern. Die Kombination einer mikroskopischen Abbildung und der optischen Kohärenztomographie (OCT) in einem einzigen Endoskop zur Verbesserung der Diagnostik scheint hierbei ein vielversprechender Ansatz, da hierdurch zusätzliche Informationen über die Beschaffenheit des untersuchten Gewebes erlangt werden können.

Das Ziel dieser Arbeit ist die Realisierung eines neuartigen Faser-Scanners für dreidimensionale OCT, dessen Design dahingehend optimiert wird, dass er zusammen mit einer Mikroskopiemodalität in einem Messkopf integriert werden kann. Durch die Verwendung eines piezolektrischen Röhrchens wird ein Faser-Scanner implementiert, der das zweidimensionale Scanmuster erzeugen kann, dass zur Realisierung von dreidimensionalen OCT-Aufnahmen benötigt wird. Der in dieser Arbeit entwickelte Scanner hat einen Außendurchmesser von 0,9 mm und eine Länge von 9 mm. Zur Kontaktierung der vier Außenelektroden des piezoelektrischen Röhrchens werden selbstentwickelte, 10 µm dicke Polyimid Flachbandkabel verwendet. Die in dieser Arbeit präsentierte OCT-fähige Demonstratorsonde ist, soweit dies durch den Autor verifiziert werden konnte, eine der kompaktesten Implementierungen eines OCT-fähigen Mikroendoskops.

Die Ergebnisse, die mit der in dieser Arbeit entwickelten OCT-fähigen Demonstratorsonde erhalten wurden, zeigen eine hohe Übereinstimmung mit den aufgestellten analytischen Modellen und Simulationen. Aus diesem Grund könnte der in dieser Arbeit beschriebene Ansatz als Vorlage für verschiedenste Sonden mit scannerbasierten Abbildungstechniken herangezogen werden.

Stichwörter: Endoskopische Sonde, bimodal, Optische Kohärenztomographie, Faser-Scanner

Abstract

Endoscopic methods play an increasingly important role in modern medicine. In general, the goal of endoscopy is to obtain as much information as possible for a viable diagnosis. To further improve diagnostics, there is a clear tendency towards multi-modal imaging by combining different imaging techniques. Making use of microscopy and Optical Coherence Tomography (OCT) in a single device is a promising approach to gather additional information and to thereby improve clinical diagnostics.

The main goal of this work is the realization of a novel fiber scanner for 3D OCT imaging, designed for its combination with a full field microscope to form a multimodal probe. A tubular piezoelectric fiber scanner is used to perform en face scanning required for 3D OCT measurements. The complete scanning engine has an outer diameter of 0.9 mm and a length of 9 mm, and features custom fabricated 10 μm thick polyimide flexible interconnect lines to address the four piezoelectric electrodes. To the best of our knowledge, the presented probe is one of the most compact implementation of an OCT microendoscope.

Optical and mechanical characterization of the scanner, implemented in a single modality demonstrator probe, show a high correlation with the analytical calculations and simulations. Thus, the approach described in this work constitutes a blueprint for a wide range of future scanning imaging probes.

Keywords: Endoscopic probe, bimodal, optical coherence tomography, fiber scanner.

Contents

1	Introduction	1
1.1	Motivation	1
1.2	State of the Art	1
1.3	Key results	3
2	Theory	7
2.1	Optics	7
2.1.1	Swept source OCT	7
2.1.2	Optical information transfer and laser scanning imaging	10
2.1.3	Laser scanning imaging	11
2.2	Mechanics of fiber scanners	14
2.2.1	Piezoelectric tube actuators	14
2.2.2	Resonant beam theory	16
3	Design & Simulation	17
3.1	Design requirements	17
3.2	Design overview	18
3.3	Optical design of the OCT beampath	19
3.3.1	Fourier plane scanner	19
3.3.2	Component selection	21
3.3.3	ZEMAX simulation	21
3.3.4	Minimization of backreflections	23
3.3.5	Single modality probe	24
3.3.6	Simulated optical performance	26
3.4	Image acquisition: spiral scanning	26
3.4.1	Driving and acquisition	27
3.5	Mechanical design	28
3.5.1	Resonance frequency calculation	28
3.5.2	COMSOL simulation	30
4	Implementation	33
4.1	Polyimide electrodes	34
4.1.1	Cleanroom processing	35
4.2	Fiber-GRIN bonding	37
4.3	3D Printed housing	37
4.4	Assembly	38

Contents

5 Experimental Evaluation	41
5.1 Fiber scanner characterization	41
5.2 Dynamic behavior of the scanner	42
5.3 Laser scanning imaging	43
5.3.1 Imaging	43
5.3.2 Lateral resolution measurement	45
5.3.3 Depth of field measurement	47
5.4 OCT imaging	48
6 Conclusion & Outlook	51
6.1 Conclusion	51
6.2 Outlook	52

Nomenclature

Latin expressions

expression	meaning
<i>distal end</i>	the part of the endoscope system which is inserted in the body, i.e. the probe.
<i>en face</i>	referring to the plane perpendicular to the optical axis
<i>ex situ</i>	performed in a different place
<i>in situ</i>	performed in the current place
<i>in vivo</i>	a study performed on whole, living organism
<i>lumen</i>	the inside space of a tubular structure, such as an artery or intestine
<i>proximal end</i>	furthest point from the distal end, i.e. the acquisition and processing system.

Latin letters

variable	meaning	unit
A	area	m^2
$b(x,y,z)$	3D image	—
C_{Rayleigh}	Rayleigh contrast	
D	diameter	m
d_{31}	piezoelectric strain coefficient	C/N
E	electric	V/m
\mathcal{F}	Fourier transform	
f	frequency	Hz
$f(x,y,z)$	3D object	
f_{res}	resonant frequency	Hz
I	light intensity	W/m^2
I	mechanical moment of inertia	kg m^2
$I[n]$	Intensity at the photodetector	A
K	truncation factor of a gaussian beam	
k	wavenumber, spatial frequency	m^{-1}

Nomenclature

variable	meaning	unit
$K_{cantilever}$	mechanical elastic constant of a cantilever	N/m
L	length	m
M	optical magnification	
m	mass	kg
N_{rings}	number of rings in a spiral	
n	sample points per ring in spiral scanning	
T	oscillation period	s
t	time	s
$u_x[n]$	Driving voltage for x axis	V
V	voltage	V
w	width	m
y	vertical displacement	m
z	axial distance	m
z_{6dB}	OCT penetration depth	m

Greek letters

variable	meaning	unit
Δk	wavenumber sweep range	
δz	axial resolution	m
ϵ	mechanical strain	
λ	wavelength	m
θ	angle	°, rad

Abbreviations

abbreviation	meaning
1D	1-dimensional
2D	2-dimensional
3D	3-dimensional
A-Scan	1D OCT measurement (usually a line parallel to the optical axis)
B-Scan	2D OCT measurement (usually in a plane parallel to the optical axis)
C-Scan	3D OCT measurement (a volume)
CFB	Coherent Fiber Bundle
DAQ	Data Acquisition System
DoF	Depth of Field
ESF	Edge Spread Function

abbreviation	meaning
FC/APC	fiber Ferrule Connector using Angled Physical Contact
FOV	Field of View
FWHM	Full Width Half Maximum
HYAZINT	Multimodal probe developed at IMTEK
IMTEK	Institute for Microsystems Engineering
lp/mm	line pairs per millimeter
LSF	Line Spread Function
LSI	Laser Scanning Imaging
MEMS	Micro Electromechanical Systems
MFD	Mode Field Diameter (of a gaussian beam)
MTF	Modulation Transfer Function
NA	Numerical Aperture
OCT	Optical Coherence Tomography
OTF	Optical Transfer Function
PSD	Position Sensitive Detector
PSF	Point Spread Function
SNR	Signal-to-Noise Ratio
SS-OCT	Swept-Source Optical Coherence Tomography
ZIF	Zero Insertion Force connector

1 Introduction

1.1 Motivation

The aging of our society is encouraging an institutional effort towards the early detection of diseases [1]. As checkups and screenings become more common, there is a need for better, less invasive diagnostic methods that reduce the risks and discomfort to the patient. An example of a common invasive procedure is histology through biopsy, used in the diagnosis of possible cancerous lesions. When the tissue is located inside a lumen, this method involves identifying the area to be sampled by endoscopy, using forceps to extract a biopsy sample and performing the histology analysis *ex situ*.

A faster and less invasive alternative is optical biopsy: a collective name for advanced endomicroscopy methods allowing real-time, *in-situ* diagnosis of tissue malignancies without the need of excision and histopathological analysis. Numerous techniques, such as endocytoscopy and fluorescence imaging, have already found their way into the clinical armamentarium over the last years; others, such as confocal laser endomicroscopy [2], Raman spectroscopy [3] or optical coherence tomography (OCT) [4,5], are expected to enter routine clinical use in the imminent future. Currently, none of these imaging modalities individually are yet to match the selectivity and specificity of traditional biopsy. This is why multi-modal imaging, which can provide complete tissue characterization through complementary modalities, will likely be the key to the success of optical biopsy.

The framework of this thesis aims to achieve optical biopsy through a compact endoscope with two imaging modalities: full field microscopy, which eases tissue identification, and OCT, which enables tomographic and volumetric imaging. The probe features a two-level design that integrates the two modalities, still allowing for independent optimization. Inside this framework, this thesis focuses on the OCT imaging device, implemented as a fiber scanner.

The next sections introduce the state of the art of endoscopic OCT and multi-modal probes followed by a summary of the key results.

1.2 State of the Art

This section summarizes the technologies that paved the way towards the multi-modal endoscopic probe developed in this project: OCT and multimodal endoscopy.

Shortly after the development of OCT technology [6], the first medical applications were reported, finding a niche in ophthalmology. But its optical sectioning abilities,

1 Introduction

allowing imaging with resolutions in tens of micrometers as seen in the example from Figure 1.1, moved soon from bench-top ophthalmology systems to endoscopic probes. The first implementations of these systems were restricted to side viewing,

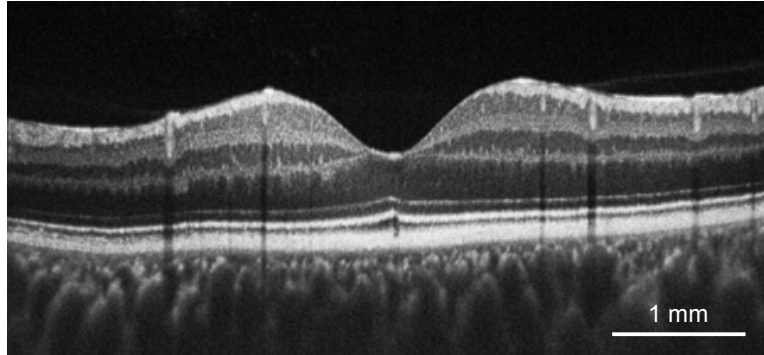


Figure 1.1: Transversal OCT image of the macula of a patient suffering from *commotio retinae* [7]

single modality OCT catheter-endoscopes that sampled the tissue by translating [8] or rotating [9] [10] the probe to acquire *in-vivo* 2D cross sections through the lumen. This scanning method, displacing the entire catheter, resulted in poor dimensional accuracy and speed. This can be solved by performing the scanning within the probe. Earlier works demonstrated this approach using Coherent Fiber Bundles (CFB) to create forward viewing endoscopes, where individual cores in the CFB were scanned sequentially to perform OCT imaging. The advantage of this method is that the scanning mechanism is located outside the body, which allows the endoscope tip to be relatively compact. As a tradeoff, the final image quality acquired with such systems suffer from poor SNR (signal-to-noise ratio) due to the CFB's multi-mode behavior and distinct inter-core coupling [11]. Furthermore, these systems are unsuitable for flexible endoscopes due to the rigidity of CFBs.

A new mechanism, the *resonant fiber scanner* [12], allowed forward-viewing video endoscopes with diameters under 1 mm within thin, flexible catheters. An example of these systems is depicted in Figure 1.2. They use the mechanical resonance of a cantilever made of optical fiber to scan a laser at video speeds. Although this scanning method can be extended to confocal endomicroscopy [13], it is challenging to implement OCT imaging, as it requires slower scanning speeds to allow the acquisition of the wavelength dependant information. Thus a method to lower the resonance frequency of the scanner is needed [14].

With the advent of MEMS technology, it became possible to integrate active micro-mirrors on the distal side of the endoscope [16]. The *Gisela and Erwin Sick Chair for Microoptics* at the *Institute for Microsystems Engineering* (IMTEK) has made recent advancements in the integration of different active scanning MEMS devices in microendoscopic probes, demonstrating OCT imaging [17].

Regarding the implementation of multi-modal endoscopic imaging systems, two major trends can be found in literature. The first of these is based on ultra-

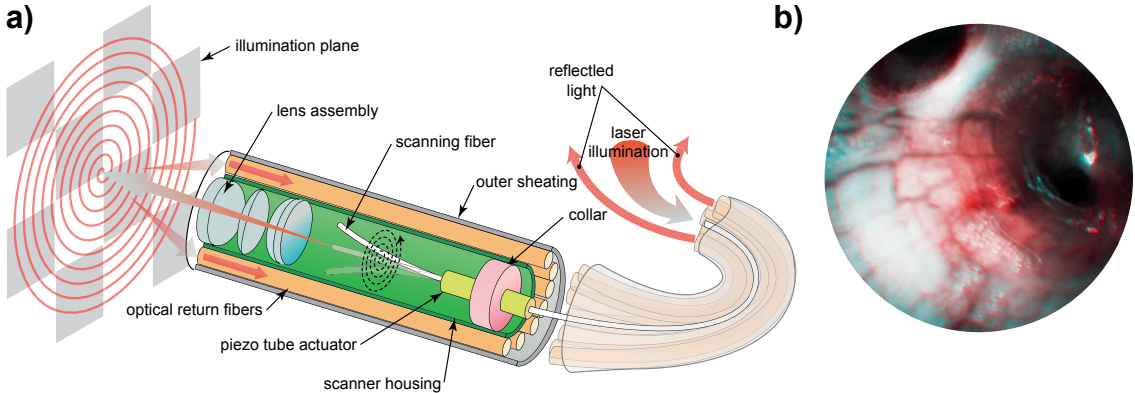


Figure 1.2: a) Functional diagram of a resonant fiber scanner for video endoscopy with the scanning illumination fiber moving in a spiral scan pattern. b) Bronchoscopic image frames from standard RGB imaging at 500-line images at 30 Hz using the probe in a) [15].

miniaturized fiber scanners and combines two confocal techniques, such as confocal laser microscopy, OCT and laser scanning fluorescence imaging [18, 19]. However, the lack of full-field video-endoscopy hinders visual guidance during the endoscopic procedure. A commercial endoscope, with dimensions usually in the centimeter range, can be used in parallel, but, as each optical system has a different axis, it is difficult to correlate both images. The second approach uses a coherent fiber bundle (CFB) to image the tissue in white-light or narrow-band illumination, while individual cores in the CFB are scanned sequentially for the confocal imaging. But, as previously described, this approach is not well suited for OCT.

A third solution was developed at IMTEK within the HYAZYNT project [20] [21] using a MEMS-based bimodal endoscopic probe which enable simultaneous full field imaging and OCT. The optical beampath of both modalities is combined before the objective lens, as depicted in Figure 1.3. The two imaging fields have the same optical axis, allowing for the registration of both images. Furthermore, the two-level design of the probe makes the integration of the two modalities possible while still decoupling their individual requirements. With the completion of the HYAZINT project, the OCT modality did not integrate a scanning mechanism to enable 3D imaging. Therefore, the aim of this work is to expand the concept demonstrated in the HYAZINT probe with the integration of a 2D fiber scanner optimized for OCT.

1.3 Key results

This thesis realizes a novel fiber scanner in a telecentric configuration which reduce the distortion in the OCT modality and enables its integration within a multi-modal probe with dimensions of $13 \times 2 \times 3 \text{ mm}^3$. The complete scanning engine has an outer diameter of 0.9 mm and a length of 9 mm, and features custom fabricated 10 μm thick

1 Introduction

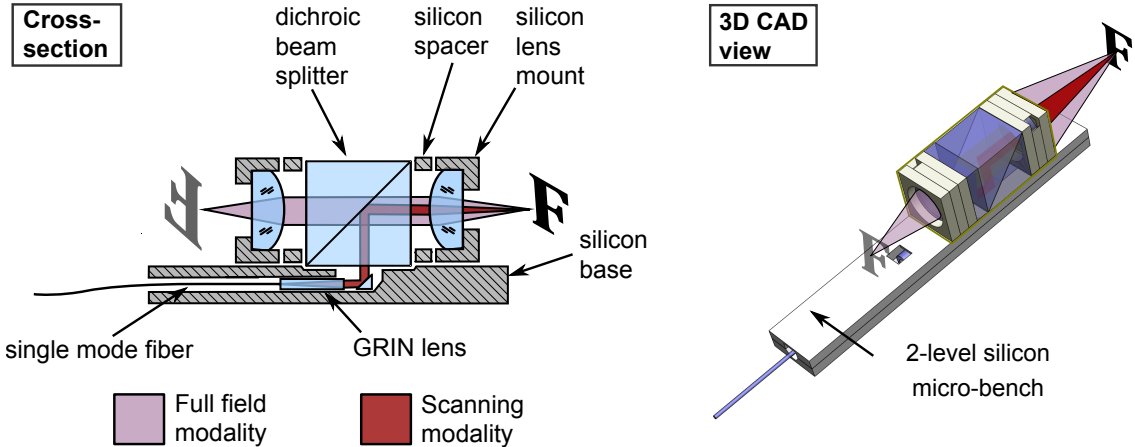


Figure 1.3: Schematic of the MEMS endomicroscope based on the HYAZINT probe [20]. Two glass lenses at each side of a dichroic beamsplitter cube form the full field microscopy beam path. A silicon aperture is used to reduce the spherical aberrations. Buried beneath the full field optics, a single mode fiber glued to a collimating GRIN lens forms the OCT channel. A reflecting micro-prism glued to a dichroic beamsplitter cube combines the two beam paths.

polyimide flexible interconnect lines to address the four piezoelectric electrodes. The small cross section of the probe combined with its short length enables its use in a wide gamut of lumens in form of flexible or tilting head endoscope.

A single modality probe was designed to independently investigate the performance of the OCT beampath. This probe, depicted in Figure 1.4a, has an external diameter of 2.5 mm and a total length of 15 mm. Its optical design emulates that of the multimodal probe OCT path, enabling a direct translation of the results from this demonstrator probe to the multimodal one. To the best of our knowledge, this single modality probe is also one of the most compact implementation of an OCT microendoscope.

Using the demonstrator probe, it was possible to obtain preliminary *en face* (Figure 1.4b) and tomographic (Figure 1.4c) images within a cylindrical volume of 1 mm diameter and 3 mm depth.

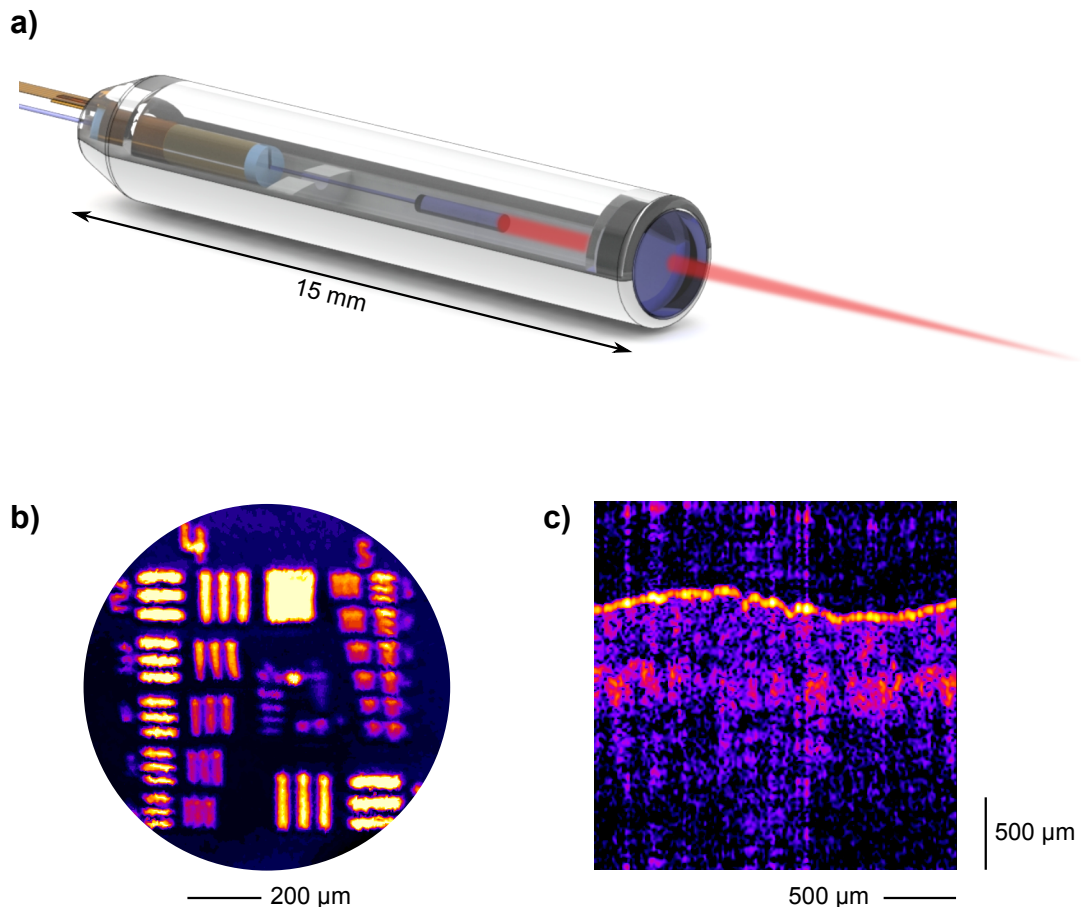


Figure 1.4: **a)** Render of the single modality demonstrator. **b)** *En face* image of a chromium-on-glass test chart acquired using laser using the demonstrator probe. **c)** OCT Image of a circular cross section of a human finger tip. Both images were obtained using the demonstrator probe.

1 Introduction

2 Theory

This work combines several principles of optics and mechanics to create an imaging system. Therefore, a review of some relevant theoretical fundamentals will ease the understanding of the design and functionality of the presented device.

Starting with the optical design, the probe uses the concept of Swept-Source Optical Coherence Tomography (SS-OCT) to extract the depth information of the sample and the mechanism of Laser Scanning Imaging (LSI) to acquire the OCT lateral information. LSI needs a scanning mechanism to displace laterally the focus position of an optical imaging device. In this work, this displacement is achieved by a tube shaped actuator which uses the piezoelectric effect to drive a thin resonant beam into resonance.

2.1 Optics

Optical Coherence Tomography (OCT) is an imaging method which allows the retrieval of depth information of a sample from its backscattered light. Due to its non-invasive nature and long working distance it found its first uses in ophthalmology, but it is currently under research in an expanding variety of medical applications.

This section briefly describes the underlying physical mechanisms of OCT. For a deeper review, a detailed analysis can be found in [22].

2.1.1 Swept source OCT

The term OCT covers several methods to extract the depth information of a sample. All of them have in common the use of an interferometer, usually in its Michelson form, depicted in Figure 2.1, to measure the coherence information.

Distance ranging with OCT: Single reflector

In Swept-Source OCT (SS-OCT), a type of Fourier Domain OCT, the light source used in the interferometer originates from a narrowband laser with the ability to tune its wavenumber $k = \frac{2\pi}{\lambda}$ over a wide range. To gain intuition on how SS-OCT can extract depth information, consider a single reflector placed in the measurement arm at a distance z_{M1} . The intensity measured by the detector due to this mirror is described by the two beam interference equation

$$I_D(k) = I_{M1} + I_R + 2\sqrt{I_{M1} I_R} \cos(2k(z_{M1} - z_R)). \quad (2.1)$$

2 Theory

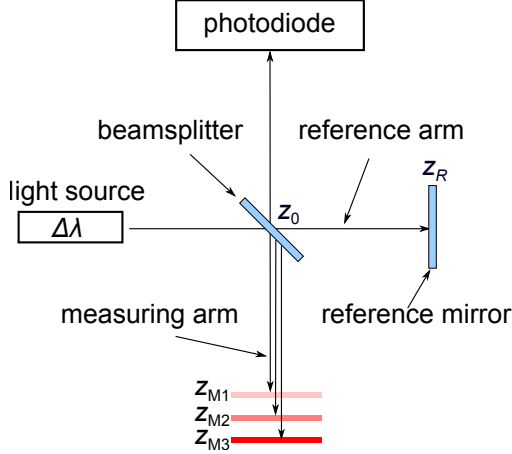


Figure 2.1: Schematic of a SS-OCT measurement system based on a Michelson interferometer, where the sample is modeled as a discrete number of reflectors at different depths and reflectivities [21]

where I_{M1} and I_R are the light intensities reflected from the measurement and reference arm. If the distance between the sample reflector and the reference mirror $\Delta z = z_{M1} - z_R$ is zero or a multiple of π/k , the intensity at the detector will be at maximum – for that particular wavenumber. If the laser source is swept across its tunable range, some wavenumbers will interfere constructively in the detector, while others destructively, happening with a period in k of $\pi/\Delta z$. This relationship between wavenumber and intensity is named spectral interferogram, and encodes the reflector position.

Depth profiling with OCT: Multiple reflectors

The same analysis can be applied to multiple sample reflectors, each one of them contributing with a modulation of the spectral interferogram with a period of $\pi/\Delta z_i$. The resulting spectral interferogram, an example of which can be seen in Figure 2.2a for 3 reflectors, can be very complex, but after decomposing its harmonic component using a fourier transform, it unveils the position of the reflectors as cross-correlations and the distances between themselves as auto-correlations, as shown in Figure 2.2b. This last plot, showing the backreflected intensity vs z-position is usually named A-scan.

Resolution and imaging depth in OCT

The ability of an SS-OCT system to resolve two reflective surfaces separated by a small z distance, termed *axial resolution* δz , improves with a wider wavenumber sweep range Δk , described in [22] as

$$\delta z = \frac{2\sqrt{\ln(2)}}{\Delta k}. \quad (2.2)$$

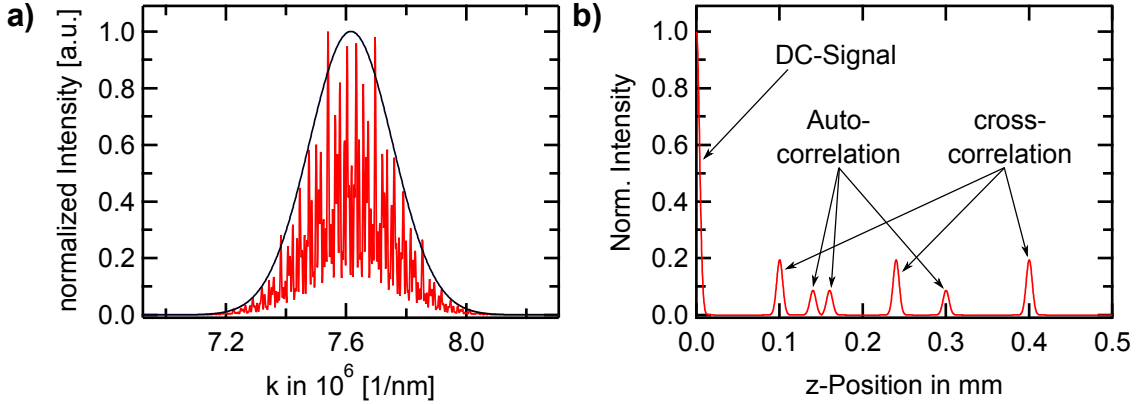


Figure 2.2: **a)** Spectral interferogram of a swept source laser with gaussian amplitude profile when used in OCT with no sample (black) and with three discrete reflectors in the sample arm (red). **b)** A-scan calculated from the spectral interferogram in *a)* using the Fourier transform. [21].

The maximum axial range or *penetration depth* that a SS-OCT can measure depends on several practical aspects. First, as seen in Equation 2.1, deep reflections are encoded as high frequency modulations in the spectral interferogram. Thus, the maximum unilateral imaging depth in air, at which the signal to noise ratio SNR is at its 6dB falloff point, is limited by the FWHM spectral linewidth $\delta_r k$ of the SS laser [22] as

$$z_{6\text{dB}} = \frac{2 \ln(2)}{\delta_r k}. \quad (2.3)$$

The collection of the backscattered light also constrains the axial measurement range. Every optical system has a certain Depth of Field DoF related to its Numerical Aperture NA and wavelength. Usually, optical systems used in OCT are designed to have a DoF longer than $z_{6\text{dB}}$ by choosing a small enough NA. The last limiting factor in the penetration depth comes from the sample itself. In biological tissue, scattering and absorption become more important with depth, lowering the chances that a photon is collected back into the OCT system.

The ability of the system to resolve two adjacent points, i.e. its *lateral resolution*, is independent of the axial resolution and completely determined by the optical system, as described in the next paragraphs.

Volumetric OCT imaging

Until now we have considered the case of a static measuring laser beam extracting the depth information or A-scan of a single column of the sample. By scanning the laser beam in a 1D line, several A-scans can be assembled in a B-scan: a 2D cross section of the sample. If now several B-scans are acquired sequentially by 2D scanning, it is possible to reconstruct a 3D volume of the sample or C-scan.

As the goal of this work is to perform volumetric imaging, a 2D scanner has to

2 Theory

be integrated in the probe. For that goal, the analysis of laser scanning imaging is summarized in the next paragraphs.

2.1.2 Optical information transfer and laser scanning imaging

OCT imaging uses a conventional optical system to illuminate the sample with a laser beam and collect the backscattered photons. As such, it is affected by diffraction effects, which perform a spatial low-pass filtering of the object, limiting the imaging resolution.

Imaging in spatial domain: The PSF

To understand this phenomenon it is useful to resort to the concept of Point Spread Function (PSF). The PSF is the 3 dimensional image that a optical system creates from an infinitesimal object. Therefore, it can be considered as the impulse response of the system. As any object $f(x,y,z)$ can be described as a set of infinitesimally small points, its image can be computed as the convolution – or blurring – of each point of the object with the PSF of the optical system [23]:

$$b(x,y,z) = f(x,y,z) * \text{PSF}(x,y,z) \quad (2.4)$$

Imaging in frequency domain: The MTF

It is also possible to describe this blurring in spatial frequency domain. Here, the imaging process is modeled as a low-pass filtering of the frequency content of the object. If the object is described by its frequency content or spectrum $F(\mathbf{k})$ and the modulation transfer function $\text{MTF}(\mathbf{k})$ describes the optical filtering, the frequency content of the incoherent image can be calculated as

$$B(k_x, k_y, k_z) = F(k_x, k_y, k_z) \cdot \text{MTF}(k_x, k_y, k_z). \quad (2.5)$$

Notice that in the frequency domain, the spectrum of the object has to be simply multiplied by the MTF of the system, instead of convolved. Thus, working in the frequency domain eases the analysis of optical systems. Furthermore, there is a simple method to estimate the resolution of a system from its MTF: the maximum optical frequency k_{Rayleigh} that a system can resolve according to the Rayleigh criterion (26% dip in the intensity) is given for $\text{MTF}(k_{\text{Rayleigh}}) = 0.152$ [21].

Relation between PSF, ESF and MTF

There is a fundamental mathematical relation between the MTF and the PSF: the MTF is the real part of the fourier transform of the PSF, i.e. the Optical Transfer Function (OTF) [23]

$$\text{OTF} = \mathcal{F}(\text{PSF}) = \text{MTF} \exp(-i\text{PTF}). \quad (2.6)$$

This relationship is exemplified in Figure 2.3, where the MTF of a gaussian PSF is shown.

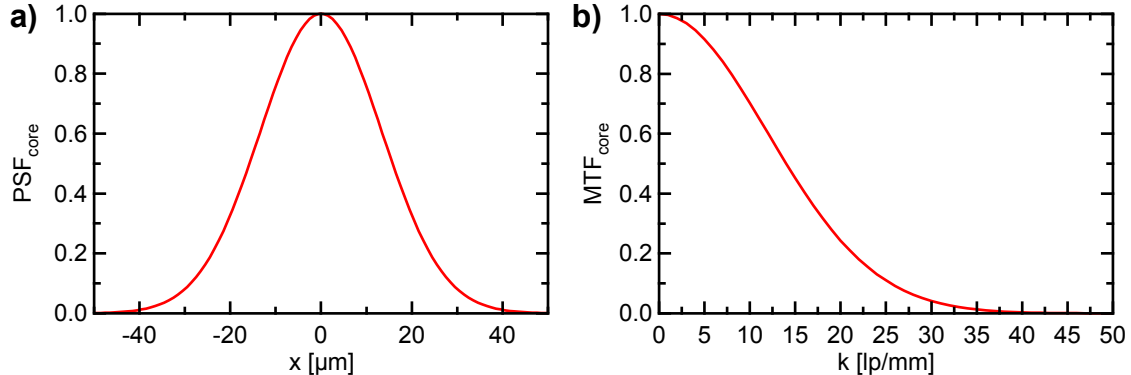


Figure 2.3: **a)** Simulated PSF of a gaussian beam focused by a lens. **b)** Corresponding MTF obtained through a fourier transform.

Measuring the PSF experimentally has the difficulty of requiring an "infinitesimally small" object to act as a *delta* function. To ease the process, it is possible to use an object with a *step* function, i.e. a sharp edge. The response of the system in this case is the two-dimensional convolution of the PSF with the *step* function

$$[\text{Step}(x)\mathbf{1}(y)] \ast\ast \text{PSF}(x,y) = \text{ESF}(x) \quad (2.7)$$

and its result denominated Edge Spread Function ESF [23]. The derivative of the ESF across x

$$\frac{d}{dx}[\text{ESF}(x)] = \text{LSF}(x) \simeq \text{PSF}(x) \quad (2.8)$$

results in the Line Spread Function LSF, which describes the result of diffraction over an infinitesimally thin line. The LSF is very similar but not equal to the PSF [23], although for the purpose of this work, this difference is safely neglected.

Thus, by simply differentiating the ESF it is possible to obtain the PSF, and by fourier tranform, the MTF of the system experimentally using the relationship described in 2.6.

2.1.3 Laser scanning imaging

After describing generally the concept of optical information transfer, these concepts are applied to the imaging topology used along with OCT to obtain volumetric images, denominated Laser Scanning Imaging (LSI). This technique, represented in Figure 2.4, uses a fiber coupled laser source to project a focused beam in the sample. Some of the backscattered light from the sample is collected back to the fiber and detected by a photodiode. By scanning the focus position through the sample using a 1D or 2D scanner, it is possible to obtain 2D or 3D images.

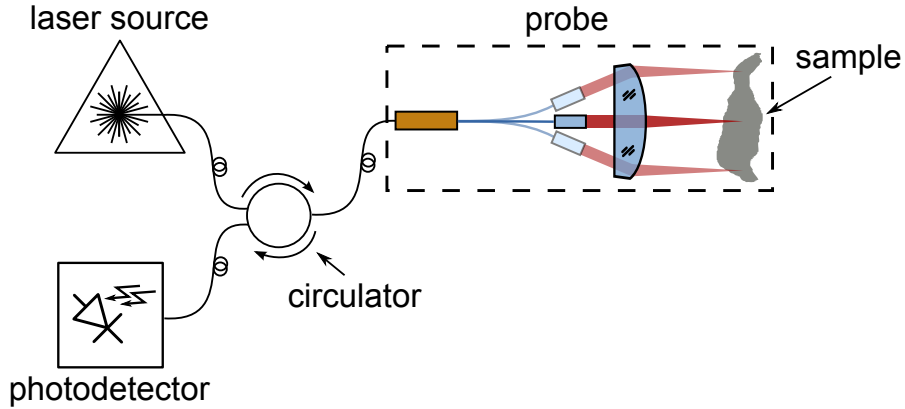


Figure 2.4: Laser scanning imaging setup. Light originating from the laser source is coupled to a probe through a circulator, while the backscattered light from the sample is coupled to the photodetector.

Modeling of LSI

To understand the optical modeling of a LSI we begin considering the probe as an illumination device, i.e. a projector. In this case, laser light coming from the optical fiber will be focused by the optical system in an object plane located at its working distance. The focused spot won't be infinitesimally small due to two reasons: first, as in any optical system, diffraction takes place and blurs it with its $\text{PSF}_{\text{optics}}(\mathbf{r})$, defined by the NA and the wavelength of the focused beam. Furthermore, the gaussian intensity distribution at the core of the fiber has a certain extent, characterized by its Mode Field Diameter (MFD). Once projected in the image plane, the MFD will be magnified by the optical system by a factor of $1/M$, where M is the magnification of the beam defined as $f_{\text{fiber}}/f_{\text{objective}}$. This gaussian spot can be conceptually considered as the PSF due to the extended core of a fiber PSF_{core} .

Thus, the projected spot, whose distribution is determined by the extended source of the fiber and the magnification and diffraction of the optical system, can be considered as the illumination PSF, calculated by convolution as

$$\text{PSF}_{\text{ill}}(\mathbf{r}) = \text{PSF}_{\text{core}}(\mathbf{r}M) * \text{PSF}_{\text{optics}}(\mathbf{r}) \quad (2.9)$$

or equivalently, the illumination MTF

$$\text{MTF}_{\text{ill}}(\mathbf{k}) = \text{MTF}_{\text{core}}(\mathbf{k}/M) \cdot \text{MTF}_{\text{optics}}(\mathbf{k}) \quad (2.10)$$

following the PSF-MTF relationship. This behavior can be observed in Figure 2.5a, where MTF_{core} and $\text{MTF}_{\text{optics}}$ are simulated according to the design values of this work.

The next step in the description of LSI considers the detection or collection of the backscattered light. If all the light coming from the fiber is projected in the PSF_{ill} , we can use the Helmholtz reciprocity property of light to state that the

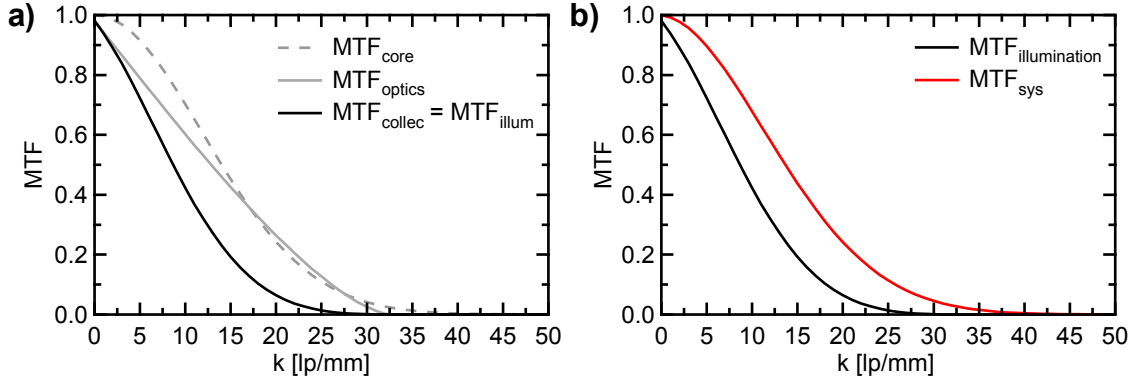


Figure 2.5: a) Simulated MTF of the illumination or collection of a single point using the proposed optical system. The collection MTF is limited by the finite size of the fiber core and the diffraction of the optical system. b) MTF of the imaging system, calculated as the convolution of illumination and detection MTFs.

photons originating within this PSF will be collected by the fiber and detected by the photodiode. Thus, the detection PSF is equivalent to the illumination PSF,

$$PSF_{\text{det}}(\mathbf{r}) = PSF_{\text{ill}}(\mathbf{r}) = PSF_{\text{core}}(\mathbf{r}M) * PSF_{\text{optics}}(\mathbf{r}) \quad (2.11)$$

or equivalently,

$$MTF_{\text{det}}(\mathbf{k}) = MTF_{\text{ill}}(\mathbf{k}) = MTF_{\text{core}}(\mathbf{k}/M) \cdot MTF_{\text{optics}}(\mathbf{k}) \quad (2.12)$$

Considering now the complete imaging process of a confocal laser scanning microscope, a photon traveling through the fiber is projected inside the PSF_{ill} , with a higher probability of illuminating the focus position. After being scattered by the sample, it has a high probability of being collected by the detector, as it is also in the center of the PSF_{det} . It can be concluded that both PSFs are multiplied together, and thus the complete imaging system PSF given by

$$PSF_{\text{sys}}(\mathbf{r}) = PSF_{\text{ill}}(\mathbf{r}) \cdot PSF_{\text{det}}(\mathbf{r}) \simeq PSF_{\text{det}}(\mathbf{r})^2 \quad (2.13)$$

or equivalently, using the autocorrelation - squaring equivalence between spatial and frequency domain

$$MTF_{\text{sys}}(\mathbf{k}) = MTF_{\text{ill}}(\mathbf{k}) * MTF_{\text{det}}(\mathbf{k}) \simeq AC[MTF_{\text{det}}(\mathbf{k})]. \quad (2.14)$$

These operations are numerically calculated in Figure 2.5b.

Finally, the resultant image can be calculated following Equation 2.4:

$$b(\mathbf{r}) = f(x,y,z) * PSF_{\text{sys}}(x,y,z). \quad (2.15)$$

2 Theory

Resolution of LSI and confocal systems

The autocorrelation of the MTF which characterizes LSI and confocal microscopy can lead to an increase in resolution compared with conventional microscopy if the illumination source and an detection aperture are significantly smaller than the diffraction limited PSF in these surfaces. In this situation PSF_{core} becomes a delta function and $PSF_{\text{ill}}(\mathbf{r}) = PSF_{\text{optics}}(\mathbf{r})$.

In this work, the pinhole is defined by the diameter of the GRIN lens, which truncates the collimated beam at its $1/e^2$ level, corresponding with a truncation factor $K = 1$. This limits the resolution of the system compared with a fully confocal system, where $K \rightarrow \infty$, as seen in 2.6.

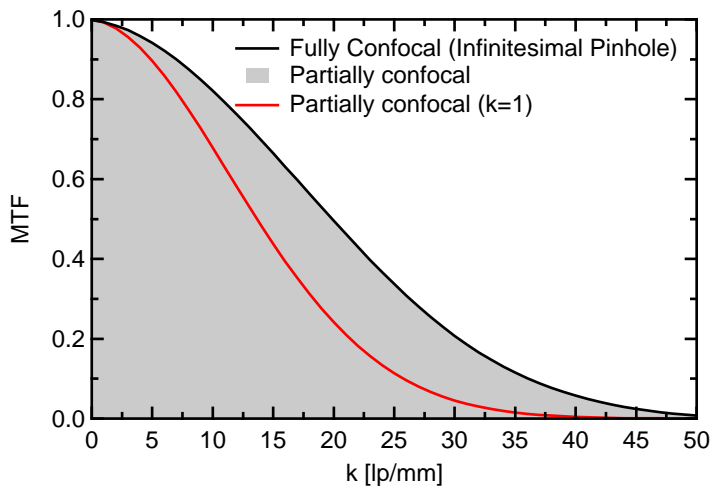


Figure 2.6: Comparison of the simulated MTF of a confocal system with infinitesimally small pinhole (black) and with a pinhole with a truncation factor $K = 1$ (red), as used in this work. The shaded area represents the possible MTFs locus for any truncation factor.

2.2 Mechanics of fiber scanners

The previous section focused in the acquisition of the depth information of a single column of a sample. But, in order to acquire a full, 3D volume of the sample, a 2D scanning mechanism is required. This section briefly goes over the physics and fundamental aspects of piezoelectric tube fiber scanners, starting with their actuation mechanism and followed by the analytical modeling of their resonant scanning fiber.

2.2.1 Piezoelectric tube actuators

A piezoelectric tube is a solid state actuator consisting of a tube made of radially polarized piezoelectric material with one inner and four outer electrodes, as depicted in

Figure 2.7a. The outer metallization of the tube is divided in four quarter electrodes,

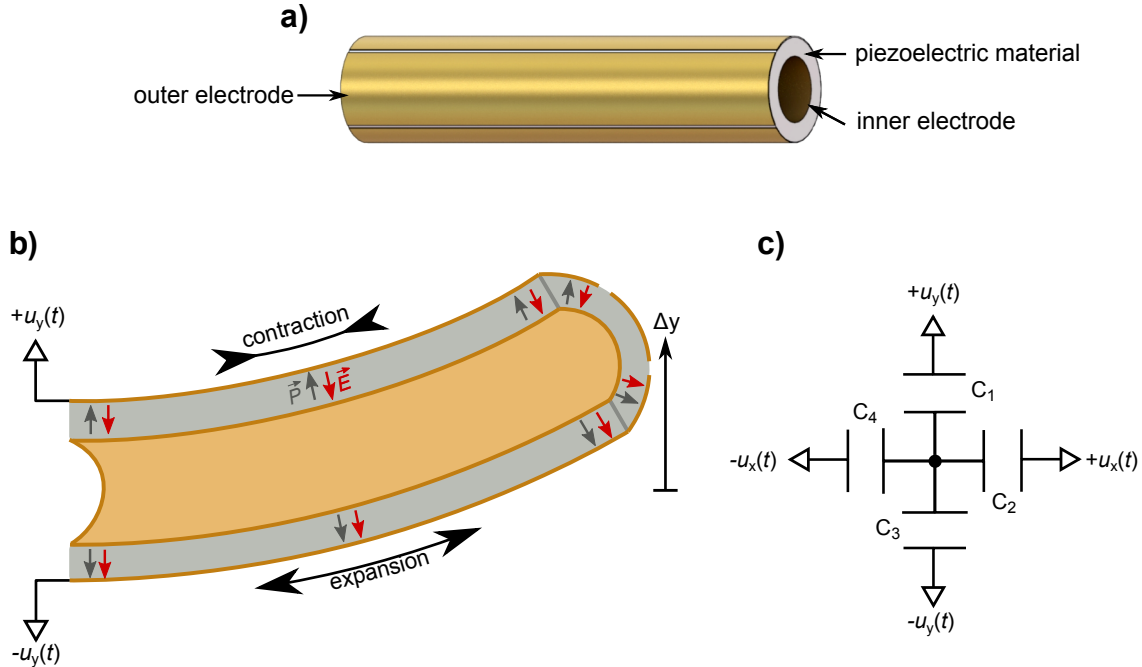


Figure 2.7: a) Render of a piezoelectric tube. b) Half-cut drawing of a piezoelectric tube in actuated state. The radial polarization of the piezoelectric material is shown in gray arrows. A voltage $\pm u_y(t)$ is applied to the top and bottom outer electrodes, creating a radial electric field under those electrodes, depicted as red arrows. Due to the piezoelectric effect, the top quarter of the tube contracts, while the bottom quarter expands, inducing a bending of the tube and a deflection of its tip $\Delta y(V)$. c) Electrical model of the piezoelectric tube with four electrodes.

which generate a radial electric field in the sandwiched portion of the piezoelectric material, shown in Figure 2.7b. If a voltage difference is applied to two opposite electrodes of the tube, one side will contract while the other will expand due to the piezoelectric effect. This behavior is modeled linearly as $\epsilon = d_{31}E$ [24], where ϵ represents the in-plane strain, d_{31} the piezoelectric strain coefficient, and E the out-of-plane electric field magnitude. This asymmetry creates a bending moment across the axis of the tube, inducing its deformation. If one end of the actuator is kept static, the tip of the actuator will deflect and tilt according to the applied voltage. A 2D scanner can be created out of this setup if two independent signals control the horizontal and vertical electrodes, as shown in Figure 2.7c.

The deflection of the tip of the tube reacts linearly with the applied voltage, and in case of bipolar operation, estimated by [25] as

$$\Delta y = V \frac{2\sqrt{2}d_{31}L^2}{\pi Dh}, \quad (2.16)$$

2 Theory

where V is the voltage applied to each opposing electrode, d_{31} is the piezoelectric strain coefficient of the material in direction perpendicular to the polarization direction, L is the length of the tube, D its outer diameter and h the thickness of its wall. Thus, longer tubes with a thinner diameter and wall thickness maximize the deflection of the tip. Typical deflections for small actuators lie in the order of 20 nm/V.

2.2.2 Resonant beam theory

The piezoelectric actuator described in the last paragraphs couples mechanical energy into the cantilever of the scanner, formed by a optical fiber segment to which a GRIN lens is glued, as depicted in Figure 2.8a. As the scanner uses mechanical resonance to amplify the small displacements of the actuator, it is important to analyze the resonance frequency of such a system.

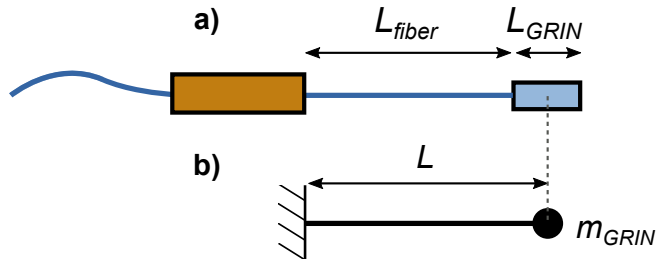


Figure 2.8: **a)** Schematic drawing of the piezoelectric scanner, composed of a piezoelectric tube, fiber and GRIN lens. **b)** Simplified mechanical diagram obtained by modeling the fiber as a weightless cantilever and the GRIN lens as a point mass.

The fiber-GRIN assembly can be modeled as a point-loaded, fixed-free cantilever where the weight of the GRIN lens is concentrated in its center of gravity, as represented in Figure 2.8b.

Now, by applying the ideal mass-spring harmonic resonator equation, the resonance frequency can be estimated as

$$f_{\text{res}} = \frac{1}{2\pi} \sqrt{\frac{K_{\text{cantilever}}}{m_{\text{GRIN}}}} \quad (2.17)$$

where $K_{\text{cantilever}}$ represents the elastic constant of the fiber cantilever. Considering it as a fixed-free, point loaded cantilever, its spring constant can be calculated as

$$K_{\text{cantilever}} = \frac{3EI}{L^3} = \frac{3\pi}{4} \frac{E_{\text{fiber}} r_{\text{fiber}}^4}{L^3} \quad (2.18)$$

following the Euler-Bernoulli theory [26] and considering that the moment of inertia of the cylindrical fiber is given by $I_{\text{fiber}} = \frac{\pi}{4}r^4$.

3 Design & Simulation

The aim of this work is to design and test a miniaturized OCT microscope as a component of a multi-modal endoscopic probe. This probe consists of two spectrally-separated optical paths that run partially in parallel through a micro-optical bench, as depicted in Figure 3.1 [21]. This approach allows independent design of the optical parameters of the two imaging modalities – such as the numerical aperture (NA) or depth of field – while still providing a geometrical overlap of the two acquired images. An integrated tubular piezoelectric fiber scanner is used to perform en face scanning required for three dimensional OCT measurements. This scanning engine has an outer diameter of 0.9 mm and a length of 9 mm, and features custom fabricated 10 μm thick polyimide flexible interconnect lines to address the four piezoelectric electrodes.

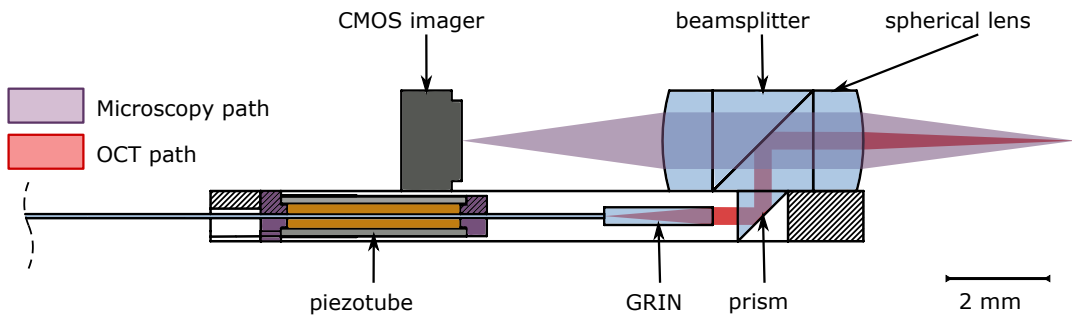


Figure 3.1: Schematic of the MEMS endomicroscope based on the HYAZINT probe [20]. Two glass lenses glued directly to the dichroic beamsplitter cube form the full field microscopy beampath. Buried beneath the microscopy optics, a single mode fiber glued to a collimating GRIN lens forms the OCT channel. The single-mode fiber is centered in a piezoelectric tube to create a fiber scanner, enabling 3D OCT. A reflecting micro-prism glued to a dichroic beamsplitter cube combines the two beampaths.

The following section describes the conception and design of the endoscope, starting from the medical and geometrical requirements, through analytical modeling and towards the optimization of each component.

3.1 Design requirements

The OCT microscope should fulfill the following requirements:

Mechanical Requirements

- The scanner, electrical connections and optics should fit in a channel with a $1\text{ mm} \times 1\text{ mm}$ cross section located in the lower level of a multimodal bench. This way the total cross section of the endoscope can be kept below $3 \times 2\text{ mm}^2$).
- Its length should be minimized to allow its integration in flexible-head endoscopes.
- The field of view should be maximized for a 2 mm diameter objective lens that is shared with the endomicroscopy beam path.
- The scanning speed should be adequate for the sampling rates characteristic of SS-OCT ($\sim 100\text{ kHz}$).

Optical Requirements

- The microscopy and OCT imaging fields should be coaxial to allow the registration of both images.
- The OCT field should be telecentric to avoid field curvature distortions.
- The lateral resolution and depth of field should be adequate for OCT i.e. with numerical aperture ranging from 0.02 to 0.05.
- The backreflections inside the probe should be minimized to reduce any loss of contrast and penetration depth.

3.2 Design overview

The main challenge of this work is to design an OCT scanning mechanism compact enough to be placed in a thin, buried channel of a multimodal probe. Although it is theoretically possible to keep a scanner at the proximal end of the endoscope and use a coherent fiber bundle as a relay, there are inherent drawbacks of this method when applied for OCT, such as low light throughput, cross-talk and mechanical rigidity [27].

Another challenging requirement is the superposition of the images acquired by the different modalities. If the optical axes are not coaxial, the fields will be shifted and tilted due to parallax error — which gains importance at the small working distances common in endoscopy.

To overcome these problems, and taking into account the above-mentioned requirements, we propose a design based on the HYAZINT multimodal probe [20]. By creating a two layer microbench, it is possible to bury the OCT resonant fiber scanner in the bottom level and merge both modalities in the top level using a dichroic beamsplitter. An schematic of this mechanism can be seen in Figure 3.1.

The base of the microbench with dimensions of $13 \times 2 \times 1 \text{ mm}^3$ is realized by standard silicon bulk micromachining. On the top layer, the bench accommodates the full field imaging optics that consists of a dichroic beamsplitter cube with dimensions of $2 \times 2 \times 2 \text{ mm}^3$ to separate the two beam paths and two plano-convex lenses with 2 mm diameter, which form a full field microscope. To achieve a highly compact opto-mechanical design, the components of the OCT beam path are buried within a cavity in the base of the micro bench. On the bottom layer a gradient index lens (GRIN lens) with a diameter of $350 \mu\text{m}$ is directly glued to the tip of a $80 \mu\text{m}$ single mode fiber to collimate the infrared light of the OCT system with a center wavelength of $\lambda_o = 1311 \text{ nm}$. A spiral scanning of the OCT beam path is achieved by an angular scanner implemented using a piezoelectric tube actuator.

This actuator, called resonant fiber scanner, is able to scan a collimated beam by more than $\pm 5^\circ$ by mechanically amplifying the subtle vibration of a piezoelectric actuator. An objective lens focuses the beam on the tissue and transforms the angular displacement into a translation. By driving the scanner in two axes with two sinusoids at different phases, it is possible to sample a 2D area of the object in a spiral fashion [28], as explained in detail in Section 3.3.

The rest of this chapter shows the design and development of the OCT imaging path for the multi-modal probe. However, in order to independently test the behavior of the OCT scanner and optics, a single modality probe was fabricated as a demonstrator. Both systems are mechanically and optically equivalent – the only difference is the presence of the beam splitter. For completeness, both multi-mode and single-mode optical systems are described.

3.3 Optical design of the OCT beampath

This section explains in detail the design of the OCT optics and its scanning mechanism. Starting with the concept of a Fourier plane scanner, the most relevant design equations are derived, which guide the selection of the optical components to achieve the desired performance, eventually verified by optical simulation.

3.3.1 Fourier plane scanner

The OCT beam path is designed as an distal-side telecentric system to avoid distortions in the 3D OCT measurement. To achieve this, the fiber scanner is driven with small angles and is positioned such that the lateral and angular movement of the scanner imitates the beam angles that can be observed in the collimated region of a classical telecentric lens system. Figure 3.2 illustrates this approach. The whole scanner is buried in a channel with an inner diameter of 1 mm limiting the movement of the scanner to a maximum angle θ of 5° that allows a maximum FOV of 1 mm of the OCT beam path.

For the scanner to work as a Fourier plane scanner, at any point of the oscillation the output beam from the GRIN lens should point to a fixed virtual radiant source.

3 Design & Simulation

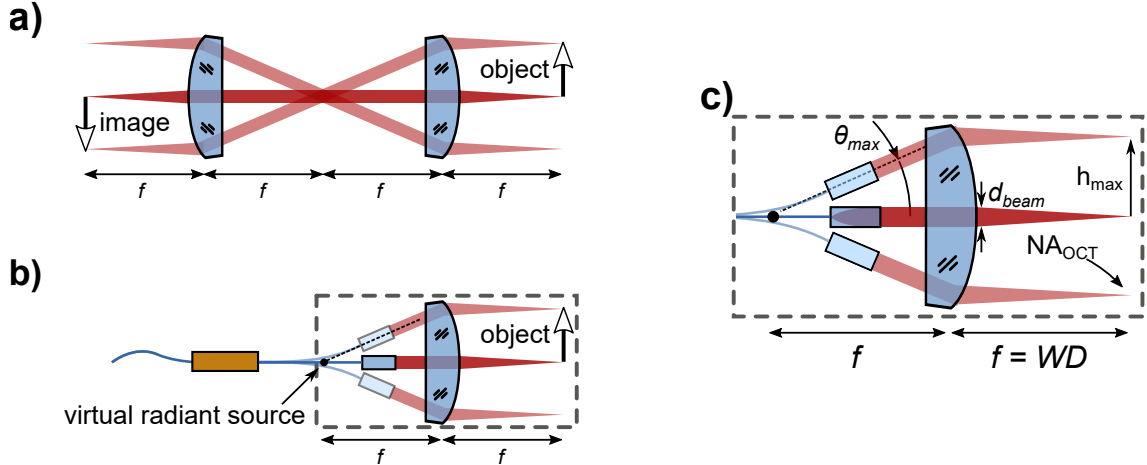


Figure 3.2: **a)** Illustration of a classical telecentric system. The height of the object is translated into an angle θ in the collimated region between the two lenses. This angle is again translated into a corresponding image height by the second lens. **b)** Illustration of the OCT beam path using a fiber scanner in first resonance mode without micro prism and beamsplitter. The movement of the GRIN lens due to the fiber scanner and the distance between the GRIN lens and the focusing lens creating the same optical behavior as it can be observed in a classical distal-sided telecentric system.
c) Nomenclature used in this work.

This is fulfilled if the bending shape of the scanner is linear with the amplitude and thus, the ratio of the GRIN lens angle to its vertical displacement is kept constant $y = d \cdot \tan \theta \simeq d \cdot \theta \Rightarrow \frac{\theta}{y} = const$ (refer to Figure 3.3). According to simulations and experimental measurements, this is the case for this implementation.

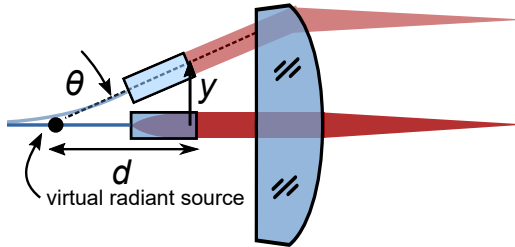


Figure 3.3: Schematic of the Fourier plane scanner at rest and at an arbitrary angle θ . If the scanner behaves linearly, the output beam will appear to come from a fixed virtual radiant source regardless of the scanning amplitude.

In a Fourier plane scanner, the numerical apertures and focal lengths of the scanning and objective lens are related by the diameter of the beam in the intermediate region between both lenses. Thus, based on the schematic of Figure 3.2c, the following geometrical optics relations are obtained: $d_{beam} \simeq 2 \cdot f_{GRIN} \cdot NA_{fiber}$ and

$d_{\text{beam}} \simeq 2 \cdot f_{\text{obj}} \cdot \text{NA}_{\text{OCT}}$. By combining them together,

$$f_{\text{GRIN}} \cdot \text{NA}_{\text{fiber}} = f_{\text{obj}} \cdot \text{NA}_{\text{OCT}} \quad (3.1)$$

the main design equation for the scanner is obtained. Note that these equations use a small angle approximation valid for small NA: $\tan[\sin^{-1}(\text{NA})] \simeq \text{NA}$. In this case, as any NA is smaller than 0.25, the error of this simplification is smaller than 2%.

3.3.2 Component selection

The design equations that were obtained in the previous section relate all the optical components together. Therefore, once the desired NA is chosen, there is only one free variable available. In this case, the major constraint is given by the commercial availability of the single mode fiber, so the selection of the rest of the components will follow from it.

The only commercially available single mode fiber working in the necessary wavelength range and with thinned cladding diameter (refer to Section 3.5) is *Thorlabs SM980G80*, with a diameter of 80 μm and with $\text{NA}_{\text{fiber}} = 0.18$ at $\lambda = 1.33 \mu\text{m}$.

In order to collimate the output from the fiber without clipping the gaussian beam in excess, a GRIN lens with an NA_{GRIN} higher than NA_{fiber} is needed. A good fit from the GRINTECH catalog is *GT-LFRL-035-024-20-CC (1550)*, with an $\text{NA}_{\text{GRIN}} = 0.20$ and $f_{\text{GRIN}} = 0.91 \text{ mm}$.

Now, by using the relation in Equation 3.1 we can design $f_{\text{objective}}$ by choosing an adequate NA_{OCT} . To preserve a high depth of field (DOF), allow enough space for the beamsplitter and a long working distance, a narrow NA_{OCT} is preferred – in the range of 0.020 - 0.025. By choosing an intermediate NA_{OCT} of 0.022, the focal length of the objective lens

$$f_{\text{obj}} = f_{\text{GRIN}} \frac{\text{NA}_{\text{fiber}}}{\text{NA}_{\text{OCT}}} = 0.91 \text{ mm} \frac{0.18}{0.022} = 7.5 \text{ mm} \quad (3.2)$$

can be selected. The manufacturing of this lens was performed by *Optik+* with a plano-convex spherical geometry, as one of the facets of the lens has to be cemented to the beamsplitter cube.

The field of view (FOV) of the OCT modality can be now calculated considering the maximum angular deflection of the GRIN lens in the tip of the scanning fiber by

$$h_{\text{max}} = f_{\text{obj}} \cdot \tan \theta_{\text{max}} = 7.5 \text{ mm} \cdot \tan 5^\circ = 0.66 \text{ mm}, \quad (3.3)$$

equivalent to a FOV of 1.2 mm for a θ_{max} of $\pm 5^\circ$, as calculated in section 3.5.

3.3.3 ZEMAX simulation

Once the components are selected, it is possible to validate the theoretical analysis of the optical design by performing a raytracing simulation. Using ZEMAX, the

3 Design & Simulation

fiber facet is modeled as the waist of a gaussian beam source, the GRIN lens is modeled using a design file from the manufacturer and the prism, beamsplitter and planoconvex lens are modeled geometrically according to the provided mechanical drawings. The result is shown in Figure 3.4.

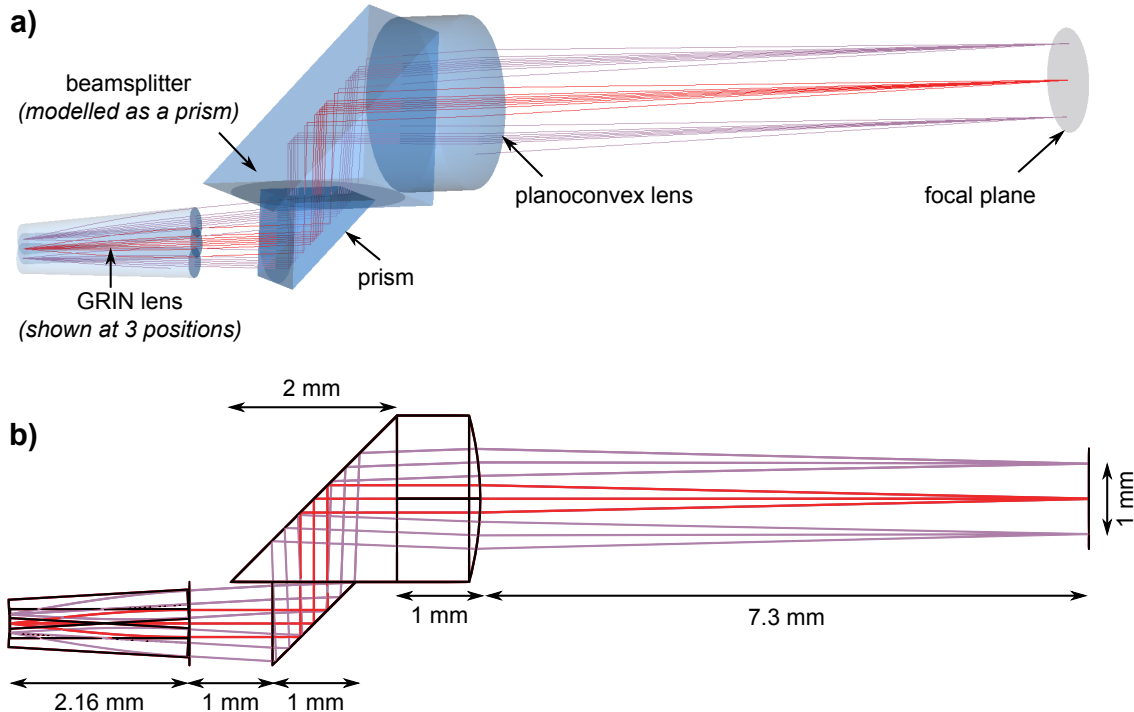


Figure 3.4: a) 3D ZEMAX raytracing of the OCT beam path for the center (red rays) and marginal (purple rays) position of the GRIN lens. Note that as the OCT beam path is reflected in the hypotenuse of the beamsplitter, it can be modeled as a 45° prism. b) Cross section of a) showing the most relevant dimensions.

The three overlapping rectangles on the left simulate the rest position (red) and maximum deflection (purple) of the GRIN lens. The gap between GRIN lens and prism is calculated so that the focus of the planoconvex lens coincides with the virtual radiant source of the scanner, creating a telecentric system.

Due to the low NA_{OCT} and the good optical quality of the GRIN and planoconvex lenses, the aberrations in this design are negligible and thus has an optical performance very close to the diffraction limit. Figure 3.5 proves this behavior by comparing the MTF (Modulation Transfer Function) of an ideal optical system with the simulated MTF of the system which is described.

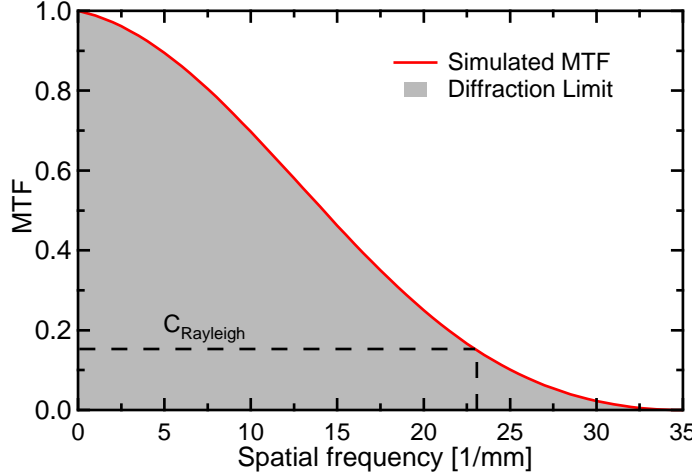


Figure 3.5: Simulated MTF curve of the OCT beam path for the bimodal probe. It can be observed that the system is diffraction limited and provides a lateral resolution of 23.3 lp/mm or 43 μm , using the Rayleigh criterion (subsection 2.1.2).

3.3.4 Minimization of backreflections

In OCT, any backreflection inside the probe increases the background intensity at the photodetector, thus limiting its dynamic range. The consequences are higher noise, lower penetration depth and lower contrast of the resultant image. Therefore any source of backreflections in the design should be carefully considered and minimized. The main sources of backreflections are marked in Figure 3.6 and explained in the following list:

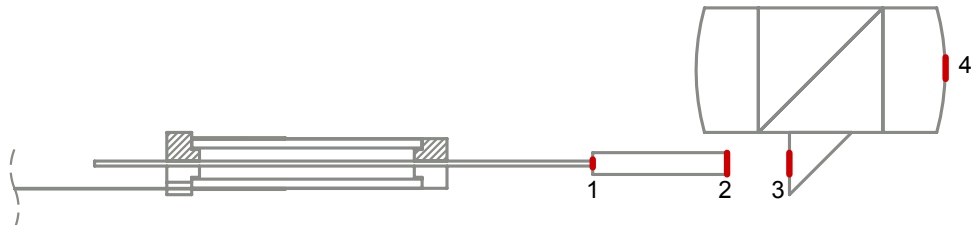


Figure 3.6: Schematic of the multimodal probe showing the main interfaces where backreflections can originate (red). 1) Fiber - GRIN. 2) GRIN - air gap. 3) Air gap - prism. 4) Objective - air.

1. **Fiber - GRIN interface:** Starting from the proximal side, the facet of the fiber and the GRIN lens are two parallel glass surfaces separated by a small gap. Although the beam is not collimated in this region, a small portion of light can be coupled back to the fiber. In order to minimize any backreflections, fiber and GRIN are glued together using a refractive-index-matched optical

3 Design & Simulation

adhesive (*NOA 76*, from *Norland Products*). This way there is no glass to air interface and the maximum refractive index step is reduced to 0.05.

2. **GRIN - gap interface:** The next interface is the distal facet of the GRIN lens. This is a critical backreflection source – regardless of the scanning angle, there is normal, collimated light incidence. To avoid this problem without resorting to delicate and expensive antireflection coatings, the GRIN lens is manufactured with a 1° tilt exit facet. According to geometrical optics, this tilt induces a vertical shift in the position of the backreflected focal point $\Delta y = f \tan(2\alpha)$ which in this system equates to $0.91 \text{ mm} \cdot \tan(2^\circ) = 31 \mu\text{m}$.

The result is visible in the simulation from Figure 3.7: the backreflected light is focused back $31 \mu\text{m}$ away, effectively missing the core of the fiber – which has a diameter smaller than $5 \mu\text{m}$.

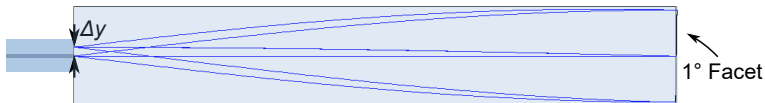


Figure 3.7: Schematic showing the raytracing simulation of a beam exiting from the distal facet of the fiber and being coupled into a GRIN lens with a tilted exit facet. The backreflected light misses the core of the fiber and is thus not coupled back to the OCT system.

3. **Air - prism interface:** Due to collimated incidence, this interface can produce important backreflections, but only in the resting position of the GRIN lens, when the free end of the GRIN lens is pointing perpendicular to the surface of the prism. To minimize reflections in this situation it is possible to resort to anti-reflection coatings in the facet of the prism.
4. **Objective lens - air interface:** After the prism, the beamsplitter and objective lens are cemented together, making any backreflections negligible. The objective lens has an interface with air, but has an anti-reflection coating on this surface. Furthermore, due to the curved surface of this lens, the backreflected light won't be focused back in the single mode fiber significantly.

3.3.5 Single modality probe

As stated in section 3.2, in order to independently test the behavior of the OCT scanner and optics, a single modality probe was fabricated as a demonstrator. Its optical design, depicted in Figure 3.8, emulates the multimodal design from Figure 3.4 by unfolding its optical path. The main difference is the lack of the prism and beamsplitter and the orientation of the planoconvex lens, which is flipped to reduce the backreflections caused by normal incidence on the planar side of the lens.

3.3 Optical design of the OCT beampath

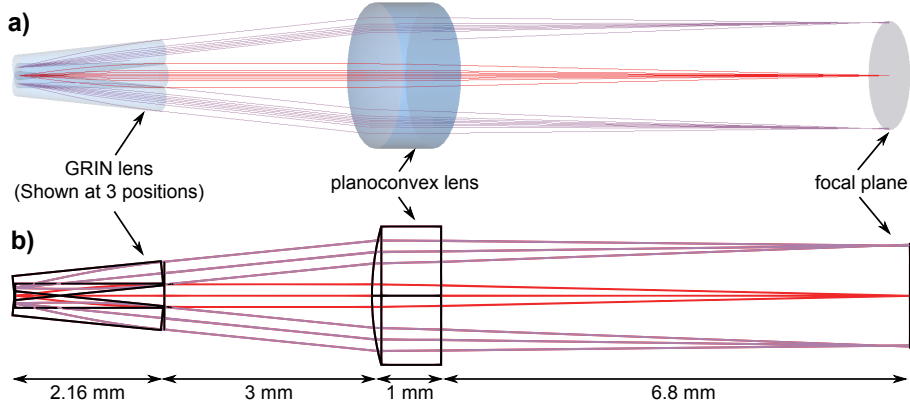


Figure 3.8: a) 3D ZEMAX raytracing of the OCT beam path for the center (red rays) and marginal (purple rays) position of the GRIN lens in the single modality demonstrator. b) Cross section of a).

The equivalence of both systems is emphasized by the similarity of their simulated MTF. Again, Figure 3.9 indicates that the single modality demonstrator is diffraction-limited.

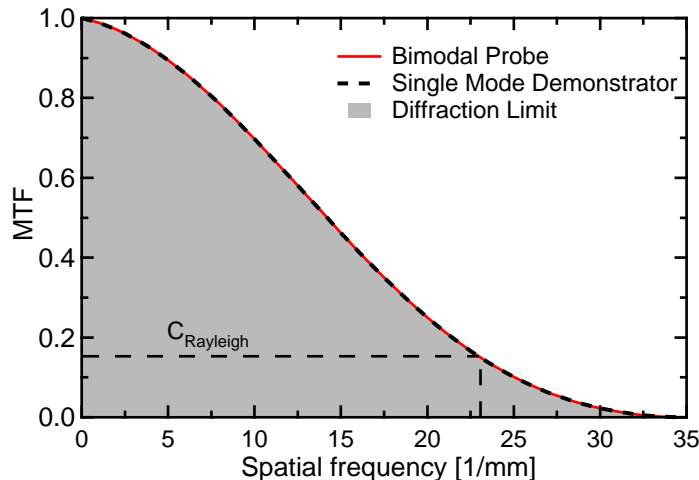


Figure 3.9: Simulated MTF curve of the OCT beam path for the bimodal probe and the single modality demonstrator. It can be seen that both implementations are optically equivalent and diffraction limited, providing a lateral resolution of 23.3 lp/mm or 43 μm using the Rayleigh criterion (subsection 2.1.2).

Due to these similarities, it is expected that any experimental result obtained with the demonstrator can be easily transferred to the behavior of the bimodal probe.

3.3.6 Simulated optical performance

To conclude this chapter, the most important characteristics of the components of the OCT microscope are listed in Table 3.1 and the simulated performance in Table 3.2.

Table 3.1: Summary of the most relevant characteristics of the optical components used in the OCT modality.

Parameter	Value
Single mode fiber NA	0.18
GRIN lens NA	0.2
GRIN lens focal length	0.91 mm
Planoconvex lens focal length	7.5 mm

Table 3.2: Simulated optical performance and characteristics of the OCT modality.
All resolution values follow the Rayleigh convention of 15.5% modulation subsection 2.1.2.

Parameter	Bimodal Probe	Single Mode Demonstrator
Distal Side NA	0.022	0.022
Working Distance	7.3 mm	6.8 mm
Field of View	1.2 mm	1.5 mm
Depth of Field	3.4 mm	3.4 mm
Lateral Resolution	43 μ m	43 μ m

3.4 Image acquisition: spiral scanning

As described in the previous section, the OCT optical setup samples the object at only a single point. Thus, the focus point has to be 2D-scanned over the surface of the sample to obtain 3D OCT images.

A very compact solution to achieve this are resonant fiber scanners. These devices use the concept of mechanical resonance to amplify the subtle movement of a piezoelectric actuator into a large displacement and angular deflection of the tip of a scanning fiber.

As any resonant system, the movement of the scanning fiber is constrained to harmonic oscillations within a frequency close to its resonance frequency f_{res} . This requirement limits the possible scanning patterns to harmonic movements at f_{res} , excluding then raster scanning, which require at least an axis working out of resonance. Then, conventional alternatives are Lissajous [29] and spiral scanning. In order to ease the reconstruction of the image, this work implements the latter.

The following pages describe the concept of spiral scanning, its characteristics, limitations and implementation.

3.4.1 Driving and acquisition

The piezoelectric tube which drives the scanner has four outer gold electrodes to control the lateral movement of the scanner, as described in subsection 2.2.1. Two independent voltage sources control the vertical and horizontal movement of the actuator by addressing the corresponding pair of electrodes. If sine and cosine signals of the same frequency f_{drive} are used to drive the scanner, the GRIN lens will oscillate in a circle of constant radius. If now the amplitude of these signals is amplitude modulated with another sinusoidal signal of frequency f_{mod} , the resultant trajectory will be spiral, as illustrated in Figure 3.10.

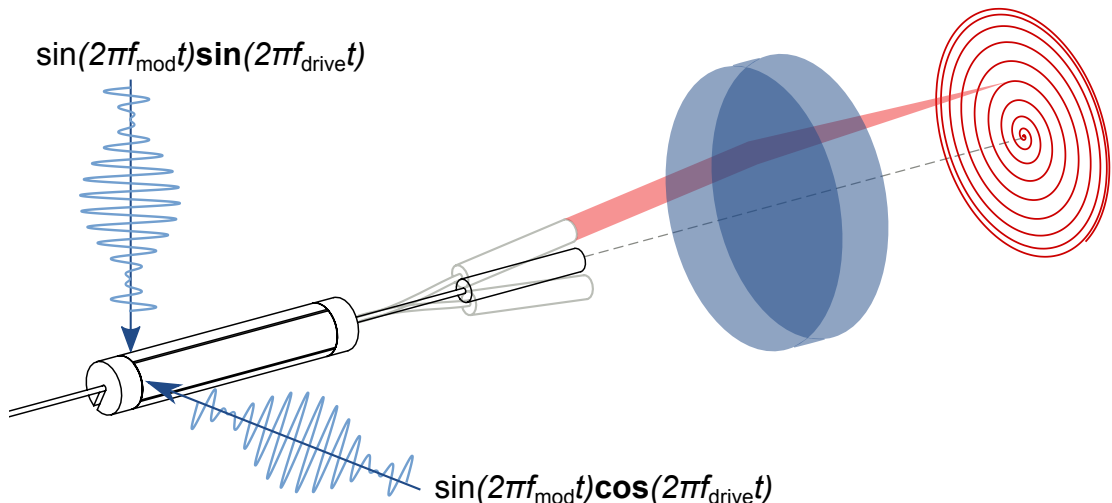


Figure 3.10: Schematic of the piezoelectric tube, fiber, GRIN and objective lens focusing the OCT beam (red) in a plane. The piezoelectric tube is driven with two independent amplitude modulated sine and cosine signals to generate a spiral pattern, used to acquire an image.

During the full period of the spiral pattern $T_{\text{spiral}} = f_{\text{mod}}^{-1}$, two complete frames are acquired, one while the spiral grows, another while it shrinks. The whole pattern can be divided in $N_{\text{rings}} = f_{\text{drive}}/f_{\text{mod}}$ individual rings, as depicted in Figure 3.11, each one acquired in a period $T_{\text{ring}} = f_{\text{drive}}^{-1}$. Thus the number of sample points that can be acquired in an individual ring

$$n = \frac{f_s}{f_{\text{drive}}} \quad (3.4)$$

depends only on the driving frequency of the scanner f_{drive} and the sampling frequency f_s of the spectrometer, which is usually constant. This value is very important, as it defines the spatial sampling density.

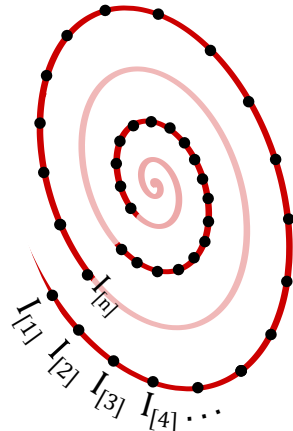


Figure 3.11: Section of a spiral trajectory highlighting two different rings. The n black dots represent the sampling points of each ring. Notice that in the inner ring the sampling density is higher than in the outer one.

In order to fulfill the Nyquist theorem, the spacing between two adjacent sample points should be smaller than the Airy radius of the laser spot. This condition is easily fulfilled in the inner rings of the spiral, where the focus spot moves at low speed. But as the radius of the spiral grows, so does the scanning speed and therefore the distance between sample points, as seen in Figure 3.11.

It is clear then that spiral scanning shows a non-uniform sampling distribution across the imaging field, which is confirmed experimentally in Figure 5.4. Thus, to avoid undersampling in the outer areas, the number of samples per ring n should be as high as possible. As OCT systems have a relatively small sampling frequency (~ 100 kHz), the resonant frequency needs to be below 1 kHz to achieve more than 100 acquired points per ring of the spiral.

3.5 Mechanical design

As explained in the previous section, in any resonant system, its geometrical and mechanical characteristics fully define the operating frequency range, and with it, constrain the way the final image can be sampled.

In the following paragraphs the behavior of the fiber scanner is mechanically modeled, and this information used to choose the most relevant fabrication parameters leading to an adequate resonant frequency for OCT.

3.5.1 Resonance frequency calculation

The scanner used in the probe consists of a piezoelectric tube which drives a beam composed of a single mode fiber and a GRIN lens into resonance, as depicted in Figure 3.12a.

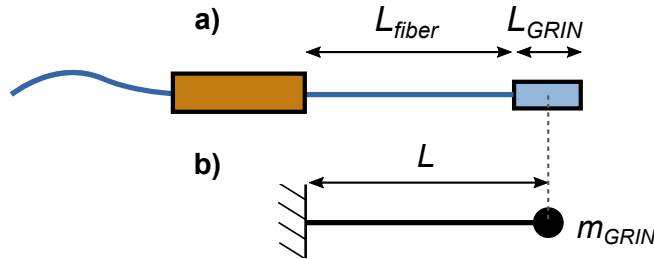


Figure 3.12: **a)** Schematic drawing of the piezoelectric scanner, composed of a piezo-electric tube, fiber and GRIN lens. **b)** Simplified mechanical diagram obtained by modeling the fiber as a weightless cantilever and the GRIN lens as a point mass.

The Euler-Bernoulli method can be used to estimate the resonant frequency of this scanner as detailed in subsection 2.2.2. The resulting equations 2.17 and 2.18 show how the different mechanical properties of the scanner influence its resonant frequency. Thus, this frequency can be reduced in different ways: increasing the cantilever length L , decreasing the radius of the fiber r_{fiber} or increasing the mass at the tip m_{GRIN} . First, by having a GRIN lens attached at the tip, the resonance frequency is reduced by a factor of 62%. Furthermore, by choosing a fiber with a cladding diameter of 80 μm instead of the standard 125 μm , the resonance frequency can be lowered by an extra factor of 60%, as the sensitivity of the resonance frequency to the diameter of the fiber is quadratic. Under these conditions, the resonant frequency vs. length of the cantilever formed by a 80 μm fused silica fiber with the chosen GRIN lens is computed in Figure 3.13 using Equations 2.17 and 2.18.

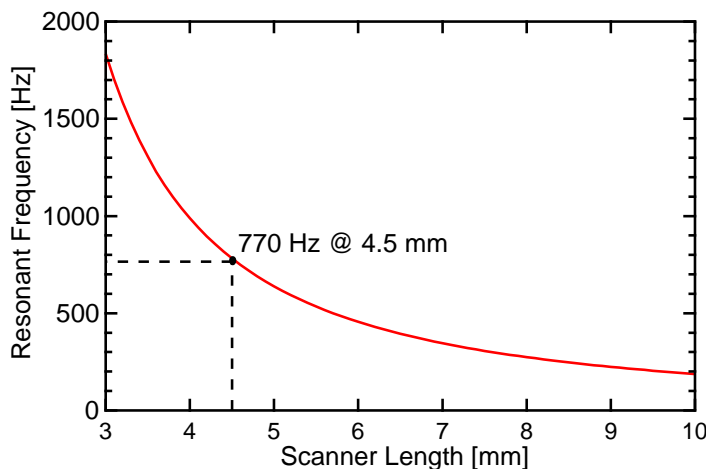


Figure 3.13: Resonant frequency of the scanner as a function of the total scanning tip length ($L_{fiber} + L_{GRIN}$). The chosen working point is labeled in the plot.

When selecting the length of the scanner, there are two details to consider. First,

3 Design & Simulation

as the scanner is buried in a 1 mm channel, the maximum displacement of the 350 μm GRIN lens is limited to $\pm 325 \mu\text{m}$. Within that small displacement we want to achieve the maximum angular deflection of the GRIN lens to maximize the FOV. This can be achieved by using shorter fiber lengths, which induces a smaller radius of curvature. This shows a trade-off with the density of sampling N_T , which is increased with longer fiber lengths. To balance those terms, we chose a total scanner length of 4.5 mm, which fulfills all the before-mentioned requirements, as Table 3.3 shows.

Table 3.3: Mechanical characteristics of the fiber scanner at its designed working point.

Cantilever length	4.5 mm
Resonant Frequency	770 Hz
Max. angular deflection	5°

3.5.2 COMSOL simulation

In order to validate the theoretical analysis of the previous section, a multiphysics finite element analysis was performed using *COMSOL*. The actuator was modeled as a radially polarized piezoelectric material (*PIC 151*) and the rest of the structure as fused silica. The excitation voltage is a sinusoidal symmetrical potential between the top and bottom electrodes of the tube. Note that, as the system undergoes small deflections, it is simulated assuming linear behavior without incurring in important deviations [30].

As the first step, the resonant frequency of the system is simulated. An *Eigenfrequency* study calculate the first mode resonance at 762 Hz, which closely matches the analytical estimation of 770 Hz. The mode shape at resonance is shown in Figure 3.14, where it can be observed that the actuator and the base of the fiber are almost static, confirming the resonant behavior of the scanner.

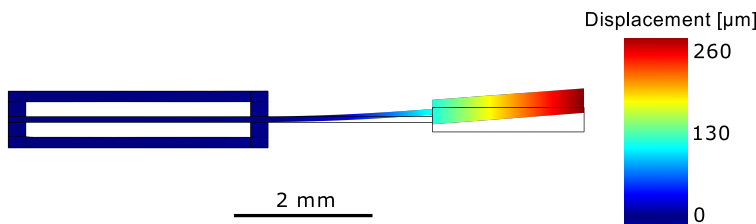


Figure 3.14: COMSOL simulation showing a cross section of the scanner maximum deflection at resonance for an actuation voltage of $\pm 75 \text{ V}$. The deformed structure is color coded showing the total displacement from the rest position (shown outlined).

Thanks to the multiphysics simulation, it is also possible to check the electric field distribution inside the piezoelectric tube. As can be seen in Figure 3.15, for a

3.5 Mechanical design

symmetrical actuation in the top and bottom electrodes with a voltage of ± 75 V, most of the volume under these electrodes experiences a field magnitude close to the expected theoretical value

$$E = \frac{U}{d} = \frac{75 \text{ V}}{150 \mu\text{m}} = 500 \text{ V/m}, \quad (3.5)$$

which is under the safe operating field of *PIC 151*, which ranges from $+1000$ V/m to -700 V/m. Only some fringe areas exceed these values, which could become depolarized with time.

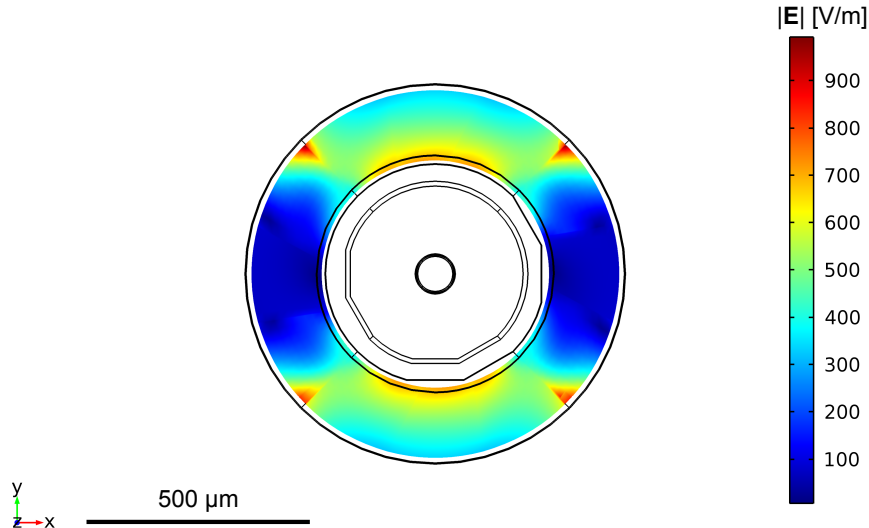


Figure 3.15: Magnitude of the electrical field inside a cross-section of the piezoelectric tube with an excitation voltage of ± 75 V applied to the top and bottom electrodes.

3 Design & Simulation

4 Implementation

This chapter details the implementation of the probe shown in Figure 4.1, which serves as a demonstrator of the fiber scanner design and evaluation tool of the optical performance of the OCT beam path.

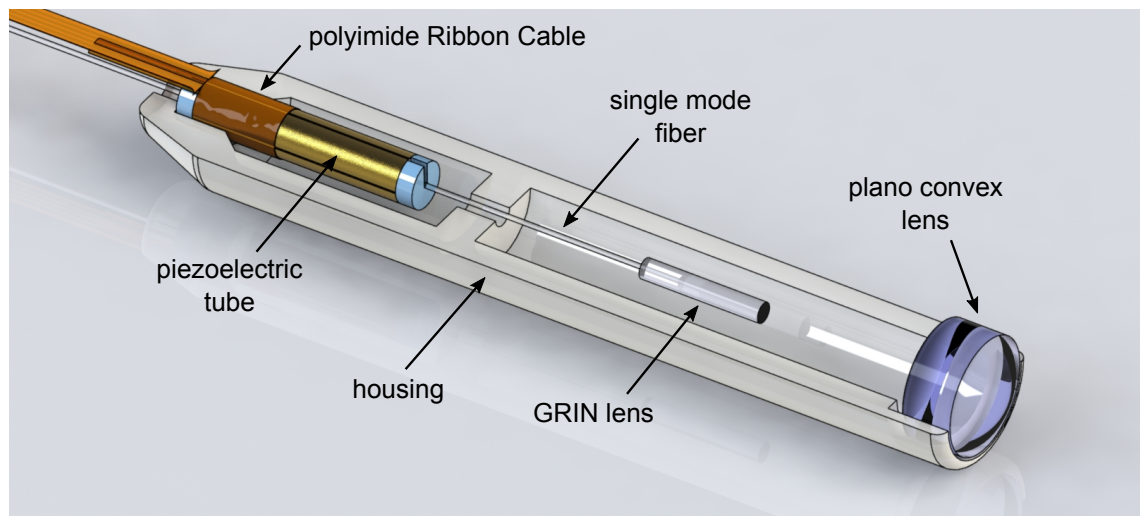


Figure 4.1: CAD of the single modality demonstrator with the top of the housing removed. Total length: 15 mm.

The design can be summarized as follows: The piezoelectric actuator has four outer gold electrodes to control the lateral movement of the scanner. The addressing of these electrodes is realized by a ribbon cable, which is wrapped around the piezoelectric tube. The single mode fiber is centered in the piezoelectric tube and the GRIN lens bonded to the tip of this fiber. This arrangement enables a compact fiber scanner with a total length of 9 mm and a resonance frequency of 750 Hz optimized for an OCT system with an A-Scan repetition rate of 100 kHz.

The following paragraphs describe the manufacturing process and assembly of the most relevant components of the probe, beginning with the fabrication of the polyimide electrodes used for contacting the piezoelectric tube and proceeding with details of the necessary assembly steps to fabricate the scanner, leading to the assembly of the complete probe.

4.1 Polyimide electrodes

The first challenge that appears in the manufacturing of the scanner lies in contacting the four external electrodes of the piezoelectric tube.

Due to the small diameter of the tube (800 µm), creating a reliable interface between the driving circuit and its electrodes is not trivial. Other piezosscanner implementations use soft soldering and insulated copper wires [13–15], but the soldering process can damage the piezoelectric material, as it is exposed to temperatures above its Curie temperature. This method also increases the diameter of the actuator significantly, as a solder blob is needed.

Instead, this design uses a polyimide ribbon cable which is wrapped around the piezotube and addresses its four external electrodes using vias. Its geometry, cross section and application over the tube is depicted in Figure 4.2, while Figure 4.3 shows its complete design.

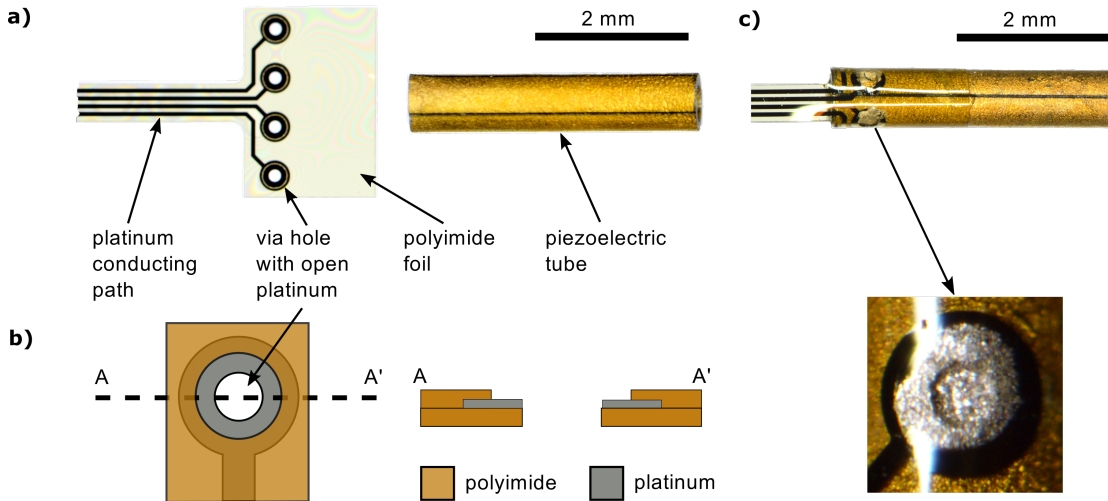


Figure 4.2: Polyimide electrode design. **a)** *Left:* Photo of the polyimide ribbon cable with four vias to contact the four gold electrodes of the piezoelectric tube. *Right:* Piezoelectric tube. **b)** Schematic of one via and its cross section. The platinum around the via is partly uncovered to improve the electrical connection between the cable and the piezoelectric tube. **c)** Photography of a polyimide ribbon cable, wrapped around the piezoelectric tube that is electrical connected through the vias by conductive glue. **d)** Microphotograph of the via after bonding with conductive glue, where a good wetting behavior can be observed.

The polyimide ribbon cables are manufactured using a cleanroom process similar to the one developed for cuff electrodes for nerve stimulation [31] and consists of platinum tracks and via holes embedded in a polyimide substrate. One end the cable is shaped to fit a zero insertion force (ZIF) connector. The other end can be rolled around the piezoelectric tube, allowing the bonding to its gold electrodes using conductive glue (Araldite 2020 with 80% wt. silver particles).

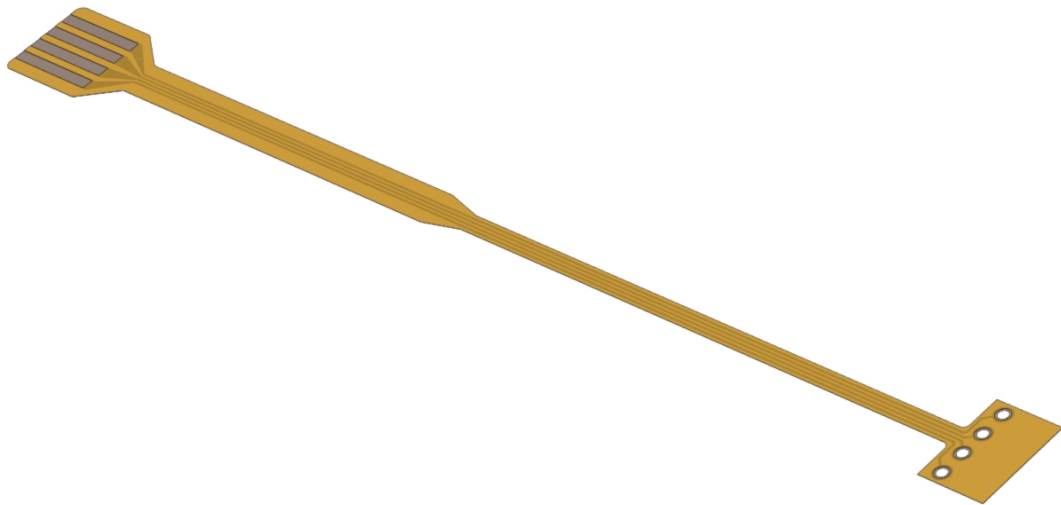


Figure 4.3: Render of a manufactured polyimide electrode. The left side fits a ZIF connector, the right side is rolled around the piezoelectric tube to address its electrodes.

4.1.1 Cleanroom processing

The polyimide ribbon cables are manufactured and singulated at wafer level. The process involves spin coating a $5\text{ }\mu\text{m}$ layer of polyimide, which is cured at $450\text{ }^\circ\text{C}$ for 10 min. Next, a 100 nm layer of platinum is sputtered and patterned via liftoff, defining the conductive traces and the bondpads. On top of it, a second $5\text{ }\mu\text{m}$ polyimide layer is spincoated and cured. Finally, the vias, openings and external shape of the cables are patterned through reactive ion etching (RIE), using the platinum as stop layer for the vias. This process is described in Figure 4.4 and the resultant wafer in Figure 4.5.

4 Implementation

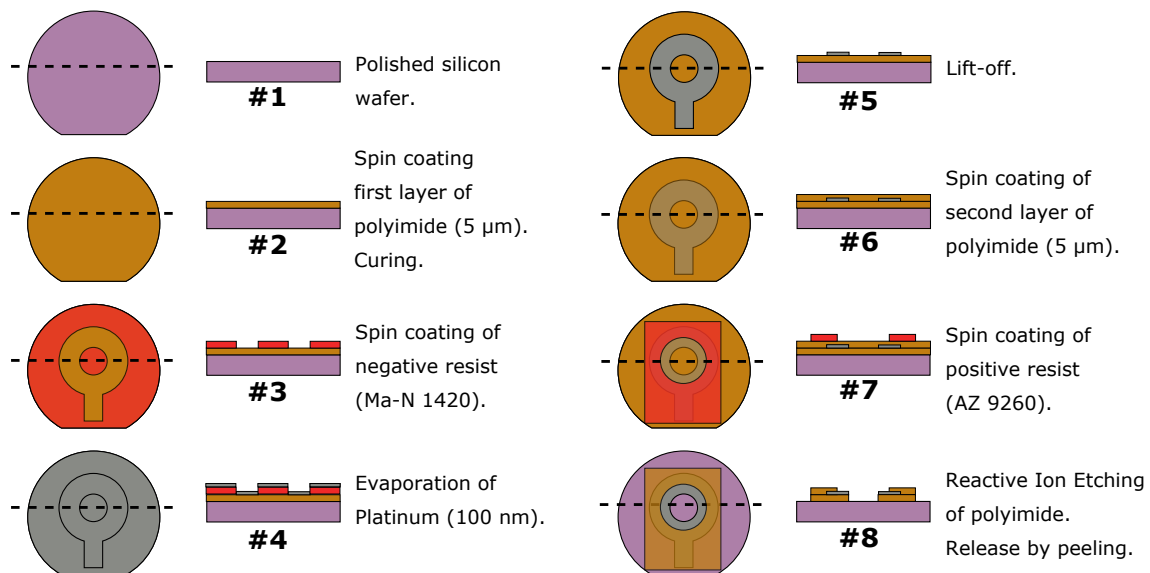


Figure 4.4: Illustration of the fabrication of a polyimide-platinum via. The first column shows the top view of the wafer, while the cross section is depicted in the second column.

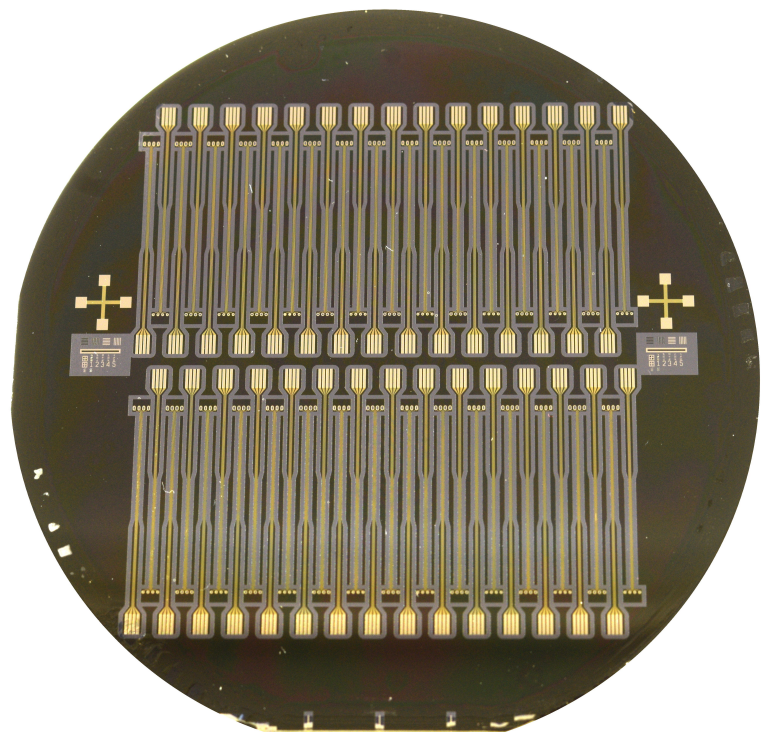


Figure 4.5: Photograph of a 100 mm wafer containing 60 polyimide electrodes.

4.2 Fiber-GRIN bonding

Another step that has to be performed before the final assembly of the probe is to optically and mechanically bond the GRIN lens to the end of the fiber . This interface is critical: first, because it is subjected to very high forces due to the oscillation of the scanner, and second, because any angular or displacement error would degrade the optical quality.

To overcome these challenges, fiber and GRIN lens are aligned together using a custom made, KOH-etched silicon alignment tool. The geometry of the KOH-etched grooves together with the cylindrical shape of both components allow the precise angle and position control of the fiber and GRIN lens. Once in place, a drop of index-matched UV-curable glue (NOA 76) bonds the components together. The wetting behavior and surface tension of the glue create a symmetrical wedge which provides extra mechanical integrity, as can be seen in Figure 4.6.

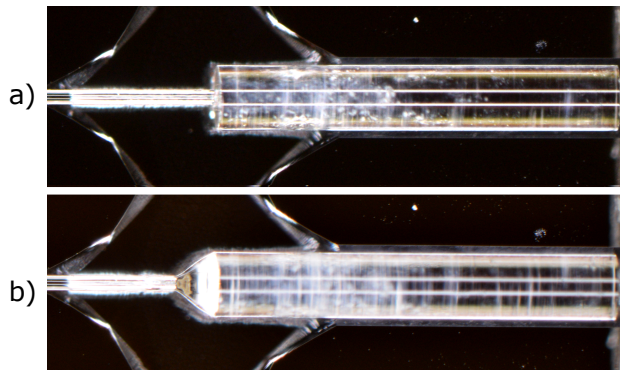


Figure 4.6: **a)** Photography of the tip of the fiber (left) and GRIN lens (right) seating in the alignment tool. **b)** Bonding with UV-curable adhesive.

4.3 3D Printed housing

The bimodal probe is designed to be assembled using the silicon bench technology [21]. But for the demonstrator, a process with reduced complexity, which allows faster design adjustments has been tested using a 3D printed polymer structure for both assembly and housing. This part was manufactured by B. Khatri (IMTEK) using a *B9Creator* stereolithography printer, which allows the polymerization of an acrylic resin with a lateral resolution of 30 μm .

This is possible because, even though the dimensional accuracy of the printed housing is lower than its silicon counterpart, the optical components of the demonstrator allow relatively high placement tolerances, as the beam is collimated in the region between GRIN lens and objective lens. This way, simple alignment structures which are 3D-printed within the housing allow the proper placement of all components, as shown in Figure 4.7. The main dimensions of the housing are depicted in Figure 4.8.

4 Implementation

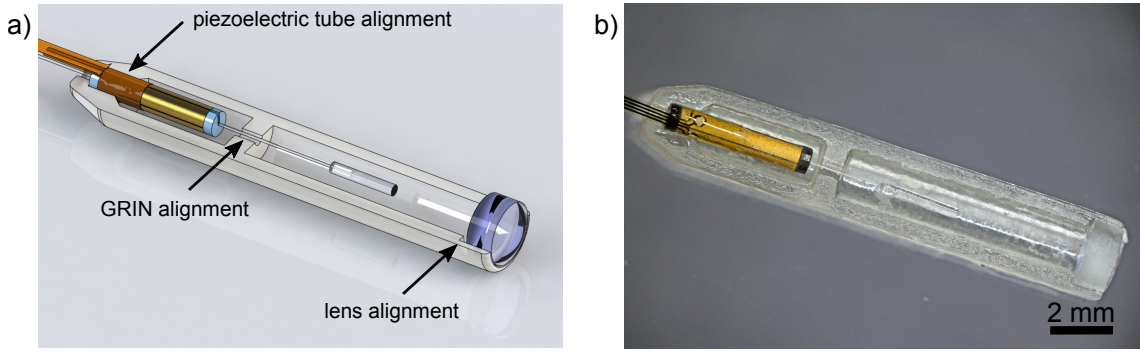


Figure 4.7: CAD (a) and photography (b) of the single modality probe with alignment features.

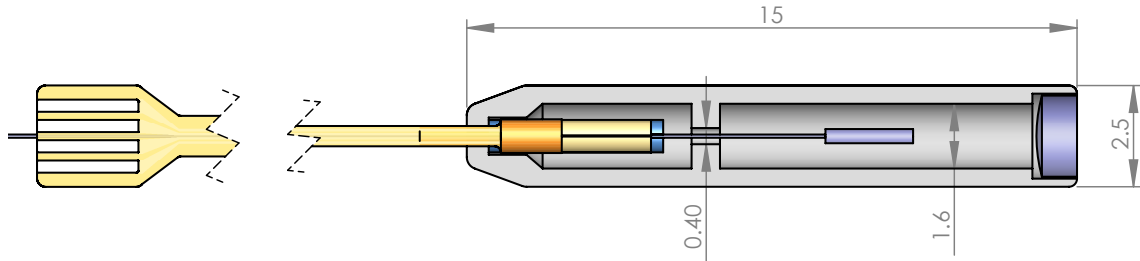


Figure 4.8: Top view of the single modality probe showing the main dimensions of the housing.

This relatively low resolution together with high part-to-part and batch-to-batch variations found in this method encourage a careful tolerance analysis during the design of the part. Nevertheless, these issues were compensated by the fast iterations in the design, allowing a successful implementation.

4.4 Assembly

Once all the components are ready, the assembly is performed manually using the multiple alignment features of the housing. The exploded view in Figure 4.9 shows the placement of the components prior to assembly, followed by the final encapsulation. This process is summarized as follows:

1. The GRIN lens is bonded to the end of the fiber using the alignment tool (section 4.2).
2. The GRIN-fiber assembly is slid through the piezotube and centered with FR-2 fittings, which are glued to the piezotube using cyanocrylate.
3. The piezotube-fiber-GRIN assembly is placed in the bottom half of the housing and glued in place using cyanocrylate with help of the alignment structures.

4.4 Assembly

4. The planoconvex lens is placed in the bottom half of the housing and glued using UV-curable optical glue.
5. The probe is closed with the top half of the housing and sealed with UV-curable glue.

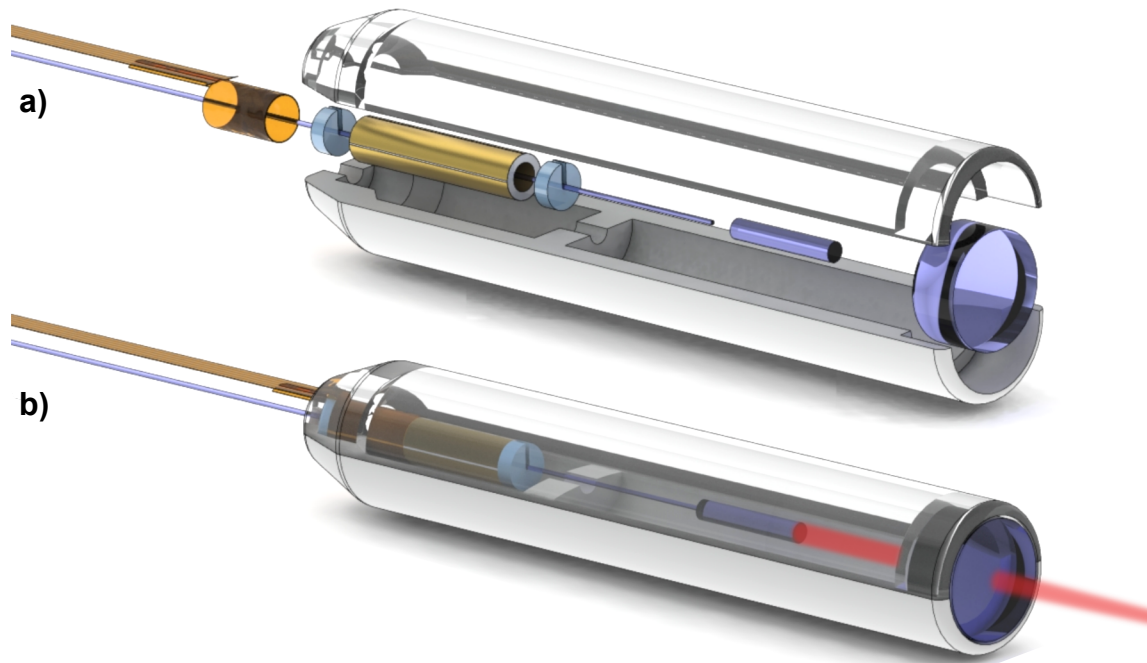


Figure 4.9: **a)** Exploded view of the components which form the single modality probe. **b)** Render of the complete probe after assembly.

4 Implementation

5 Experimental Evaluation

The following pages describe the performance of the OCT scanner demonstrator probe. First, the optomechanical characteristics of three manufactured probes are compared with their expected values. Later, a set of driving parameters optimized for each probe is used to image a sample using spiral scanning. The challenges and solutions associated with this method are discussed, highlighting the different data processing methods. Eventually, OCT measurements of biological samples are presented.

5.1 Fiber scanner characterization

Three single modality demonstrator probes were assembled to test the repeatability of the process. For each probe, a characterization step was performed in order to measure its resonance frequency, laser coupling efficiency, backreflectivity and maximum unobstructed field of view. These results are summarized in Table 5.1.

Table 5.1: Optomechanical characteristics of three assembled single modality probes compared with their expected values, calculated for a cantilever length of 4.5 mm.

	Design Value	Probe 1	Probe 2	Probe 3
Cantilever Length [mm]	4.5	4.45	4.44	4.10
Field of View [mm]	1.3	1.1	1.2	1.2
Resonant Frequency [Hz]	762	744	765	842
Coupling Efficiency	-	0.53	0.61	0.58
Backreflectivity [%]	-	0.011	0.004	0.018

- **Cantilever Length:** The cantilever length was varied between 4.10 mm and 4.45 mm to test the behavior of the scanner under different parameters.
- **Field of View:** At a certain scanning amplitude, the laser beam becomes shadowed by the edges of the optical components. In the case of the single modality probe, this happens due to the walls of the housing, which by design limit the FOV to 1.3 mm. Any misalignment between the optical axis of the scanner and the symmetry axis of the housing further reduces the FOV due to decentering.

5 Experimental Evaluation

- **Resonant Frequency:** The resonance frequency was measured by driving the scanner with a sweeping sinusoidal signal and observing the amplitude of oscillation. An example of such response can be seen in Figure 5.2. The variability of the cantilever length explains the change of the resonant frequency: shorter cantilevers exhibit higher resonance frequency, as their stiffness is higher. It can be seen that for Probes 1 and 2, whose cantilever length is close to the designed 4.5 mm, their resonant frequency is within 3% of the expected 762 Hz.
- **Coupling Efficiency:** This value was calculated by measuring the intensity of the beam exiting the probe divided by the power of the light source at its output fiber connector. Thus, it includes the losses from the FC/APC fiber connector, fiber interfaces and backreflections. It is believed that the main source of loss is the connector, which has variable losses up to 30%, depending on the quality of the polishing of the fiber facet and any surface imperfection or contamination.
- **Backreflectivity:** In order to measure the backreflected light intensity it is necessary to send and receive light through the scanning fiber. To achieve this, is it possible to reuse an OCT measurement setup with some modifications. As seen in Figure 5.1, broadband infrared light with a center wavelength of $\lambda_o = 1311$ nm and a bandwidth of $\Delta\lambda = 90$ nm from an SLED is coupled to a circulator, which forwards it to the probe. Any light which is backreflected inside the probe, together with backscattered light from the sample is coupled back to the fiber and forwarded by the circulator to the photodetector. In case that the probe is pointing to empty space, only light backreflected from the optical components is measured. By dividing this intensity by the source intensity and taking into account the coupling efficiency of the system, the backreflectivity was measured to be well controlled under 0.02%. The variability within probes can be attributed to differences in alignment and gluing of the fiber and GRIN lens or connector backreflections.

5.2 Dynamic behavior of the scanner

The use of fiber scanners for imaging involves the challenge of whirling, identified already in the first fiber scanner implementations [12].

This effect can be explained as follows: If a cantilever is rotationally symmetric, it will exhibit a single transversal resonant frequency. In this case, according to linear theory, if the base is excited in only one plane, the fiber will also only vibrate in that plane. But if a cantilever shows a small misalignment or non symmetric cross section – as expected in any real world implementation – it will exhibit two different frequency responses with peaks f_x and f_y , corresponding to two planes of symmetry or eigendirections x,y , as can be seen in the example from Figure 5.2a. Far away from resonance the difference between axes is minimal. But close to resonance, these

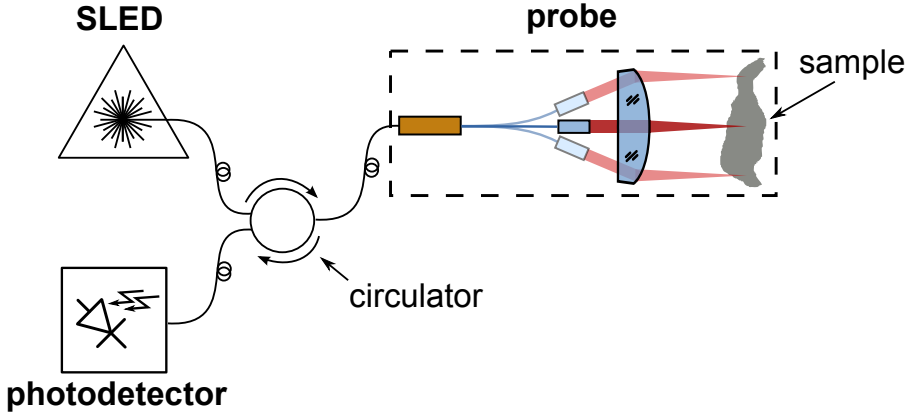


Figure 5.1: Setup used to measure the backreflectivity of the probe and for fiber-optical confocal scanning microscopy. Light originating from the SLED is coupled to the probe through the circulator, while the backscattered light from the probe and sample is coupled to the photodetector.

nonlinear effects create a cross-plane instability in which excitation of the base of the resonator in the x direction can lead to oscillations in both x and y directions. This effect can be seen in the whirl plots of Figure 5.2b.

Therefore, for the imaging experiments, the scanner operates at a working point WP far away from the resonance, in order to minimize the effect of whirling, but with a gain high enough to achieve the required amplitude of oscillation.

5.3 Laser scanning imaging

This section explains how it is possible to use the single modality probe for laser scanning imaging (LSI) and use the acquired images to assess its lateral resolution and depth of field. As OCT uses the concept of LSI to recreate volumetric images, these results are also representative for OCT imaging.

5.3.1 Imaging

The setup used to measure the backreflectivity of the probe, shown in Figure 5.1, can be used directly for LSI. While the probe scans an object with a spiral pattern defined by the driving voltage datapoints $(\mathbf{u}_x[n], \mathbf{u}_y[n])$, the data acquisition system (DAQ) samples a stream of intensities at the photodetector $\mathbf{I}[n]$, as shown in Figure 5.3a. As these signals are generated and acquired synchronously, we expect that the intensity $\mathbf{I}[i]$ corresponds to a point in object space linearly related to the driving voltage of the piezoelectric scanner: $(x, y) = K_{\text{mech}}(\mathbf{u}_x[i], \mathbf{u}_y[i])$, where K_{mech} is a mechanical constant.

If all the datapoints $\mathbf{I}[n]$ acquired during a full spiral are plotted as a intensity-coded dot located at the position $K_{\text{mech}}(\mathbf{u}_x[n], \mathbf{u}_y[n])$, the resultant image would

5 Experimental Evaluation

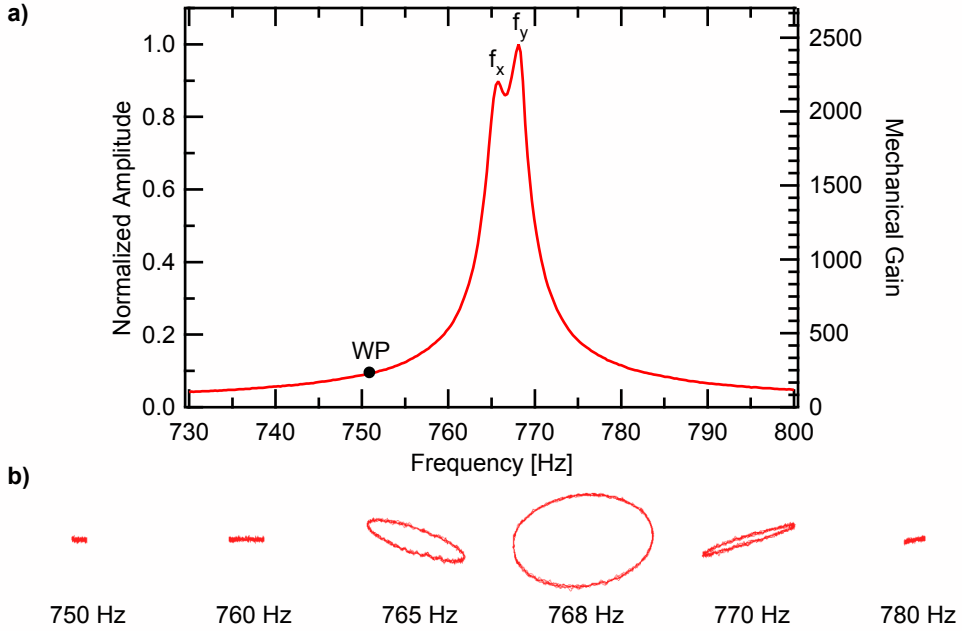


Figure 5.2: **a)** Dynamic behavior of the scanner in *Probe 2* under harmonic excitation. The two eigenfrequencies corresponding to the main axes of the scanner are marked as $f_x = 765.8$ Hz and $f_y = 768.1$ Hz. The Working Point WP shows a gain of 220. The right axis shows the mechanical gain due to resonance, defined as the ratio of the displacement of the GRIN tip to the displacement of the piezoelectric tube tip. **b)** Whirl patterns obtained by exciting the scanner in the x direction with different harmonic frequencies while measuring the position of the fiber tip.

look as in Figure 5.3a: distorted. Notice how the dot plot defines two overlaid whirling images. This proves that the previous assumption of linearity is not valid, and thus the relationship between $(\mathbf{u}_x[i], \mathbf{u}_y[i])$ and $(\mathbf{x}[i], \mathbf{y}[i])$ is neither linear nor simple. This is the result of whirling, as discussed in section 5.2. There are two general methods to overcome this problem:

The first one involves closed loop operation, where the current position of the scanner is measured inside the probe and used by the plotting system to correct for the distortion [32].

The open loop alternative, used in this work, assumes that the distortion pattern is constant for a given driving signal. Then, the distorted spiral pattern $(\mathbf{x}[i], \mathbf{y}[i])$ can be measured after the assembly of the probe using a position sensitive device (PSD) and stored as a calibration lookup table. Once this calibration step is performed, any further frame is plotted by assigning a position $(\mathbf{x}[i], \mathbf{y}[i])$ to every measured intensity $\mathbf{I}[n]$, as depicted in Figure 5.3b, resulting in a distortionless dot plot. This procedure can be performed in real time.

The dot plots which are obtained from spiral scanners have the inconvenient of

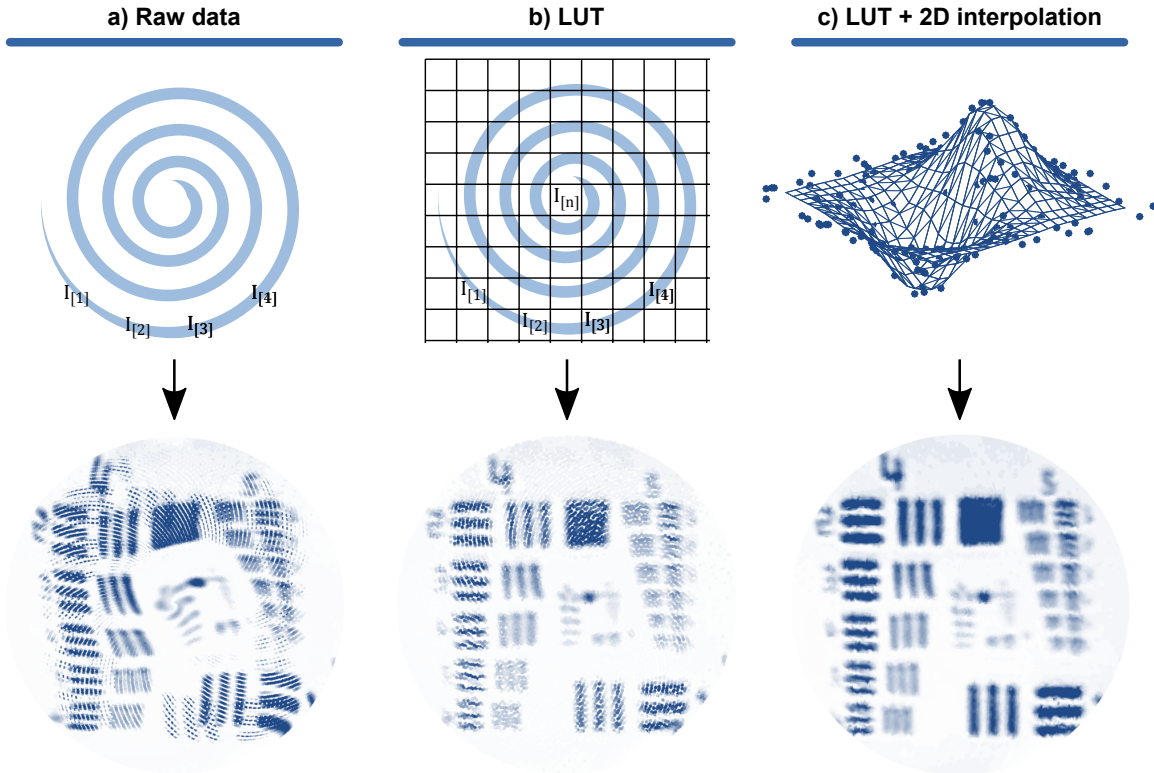


Figure 5.3: Different representations of the same acquired datapoints $I[n]$ of a USAF 1951 resolution test chart. The full acquired spiral consists of 374 rings of 122 datapoints, adding up to 45500 datapoints measured at 91 kHz during 500 ms. The field of view is 1.1 mm.

a: Point cloud assuming ideal movement of the scanner. **b:** Point cloud after correcting the position of each dot using a lookup table. **c:** Raster image after performing a 2D interpolation from the data in d.

non-uniform sampling, as can be seen in Figure 5.4. Thus, to ease the further processing of the acquired images, it is beneficial to convert the non-uniform dot plot into a cartesian raster image. This can be performed by 2D interpolation, resulting in Figure 5.3c.

5.3.2 Lateral resolution measurement

The optical performance of the scanner is qualitatively evaluated by capturing a SLI image of a USAF 1951 resolution test chart with a spiral scanning pattern using the setup described in Figure 5.1. As can be seen in Figure 5.3c, element 4 of group 4 is resolved, indicating a resolution of 22 line pairs/mm or 45 μm .

A more robust method for the calculation of the optical resolution is detailed in section 2.1.2: by manually scanning the focus of the probe over a sharp chromium edge of the test chart, the edge spread function (ESF) shown in Figure 5.5a is obtained. By performing a spatial derivative followed by a Fourier transform of

5 Experimental Evaluation

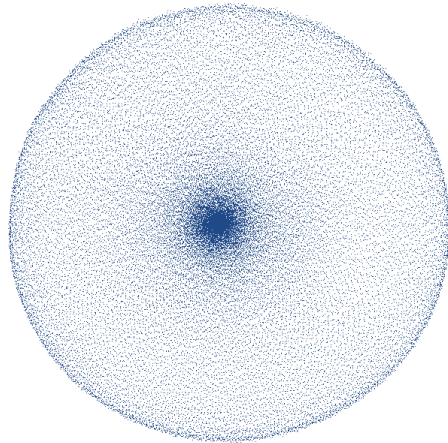


Figure 5.4: Sampling points of the scanner during a complete spiral cycle measured using a PSD. Notice the non-uniform sampling. Each one of the 45500 dots represents a sample point in object space. The coordinates of each point ($\mathbf{x}[i], \mathbf{y}[i]$) are used in a LUT to correct for the inherent sampling distortion characteristic of fiber scanners.

the ESF, the MTF can be obtained, plotted in Figure 5.5b. Based on this curve the lateral resolution of the OCT beam path was determined at 21 line pairs/mm or $47.6\text{ }\mu\text{m}$. This value is very close to the theoretical resolution, calculated in subsection 3.3.3 as 23.3 line pairs/mm or $43\text{ }\mu\text{m}$. A good concordance is observed

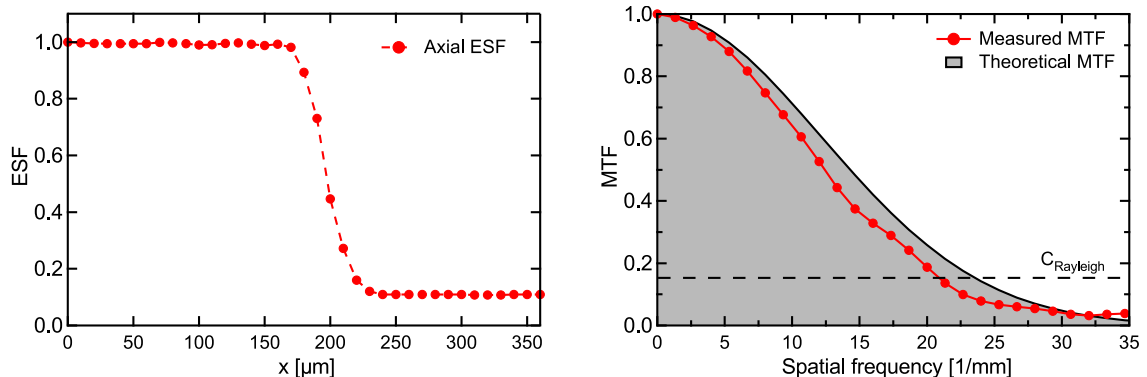


Figure 5.5: Left: Measured edge spread function (ESF) of the OCT beampath for the center of the field of view. Right: Corresponding MTF compared with the theoretical limit using the theory from subsection 2.1.3.

between the shape of the analytical and the measured MTF curves of the scanning modality. However, the overall performance is reduced by 10% compared to the simulation. This deviation can be explained by small misalignments of the optical components induced by the process tolerances of the 3D-printed housing and the assembly process. Since a better alignment can be achieved in the silicon micro bench due to the higher precision of the MEMS processes a better match between

simulation and reality can be expected for the multimodal probe.

5.3.3 Depth of field measurement

The depth of field (DOF) of the OCT imaging system can be determined by measuring how much light is backreflected upon a mirror while displacing it through the z axis. The results from this experiment are plotted in Figure 5.6, where a full width half maximum (FWHM) DOF of 3.5 mm is calculated.

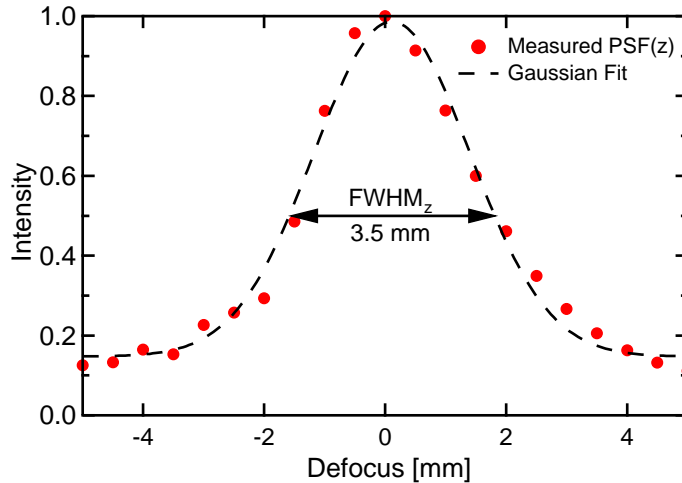


Figure 5.6: Measurement of the axial resolution of the single modality probe. The intensity of the light coupled back into the optical system after reflection on a mirror is plotted against the manual translation of the mirror by ± 4.5 mm from the focal plane of the probe.

5.4 OCT imaging

The OCT characterization was performed using a swept-source OCT system property of the Medical University Vienna. This system, represented in Figure 5.7 operates with a center wavelength of $1.34\text{ }\mu\text{m}$, a bandwidth of 37 nm and a theoretical axial resolution in air of $26.9\text{ }\mu\text{m}$.

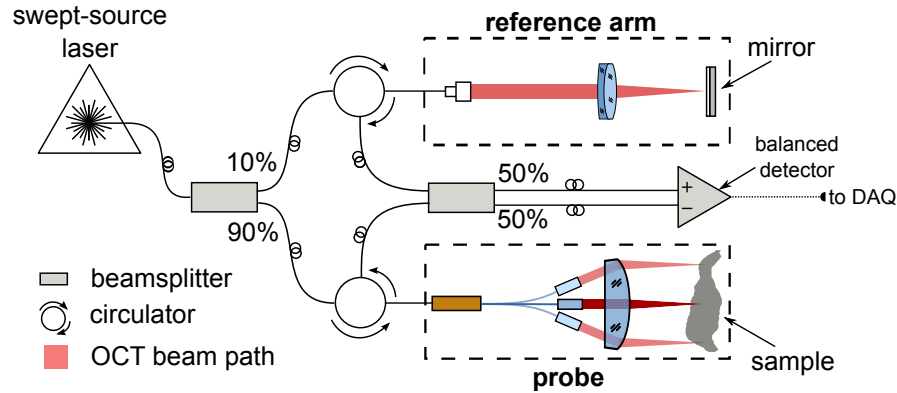


Figure 5.7: Medical University Vienna swept-source OCT system. Light originating from a swept-source laser is coupled to a balanced interferometer, where the optical path difference between the sample and the reference arm creates an interferogram which is converted to an electrical signal in a balanced detector.

The first OCT tests were performed as a proof of concept. Circular B-Scans of a colon polyp and a fingertip were captured with the single modality demonstrator, shown in Figure 5.8. These preliminary results prove that OCT imaging is possible. But at the same time, the low SNR of these images indicate that the designed system, which has a NA of 0.022, has problems collecting enough backscattered light. Therefore, future implementations of the probe could benefit from a higher NA. In that case, the resolution and collection of light of the system would be increased at the cost of a shorter working distance and a shorter depth of field.

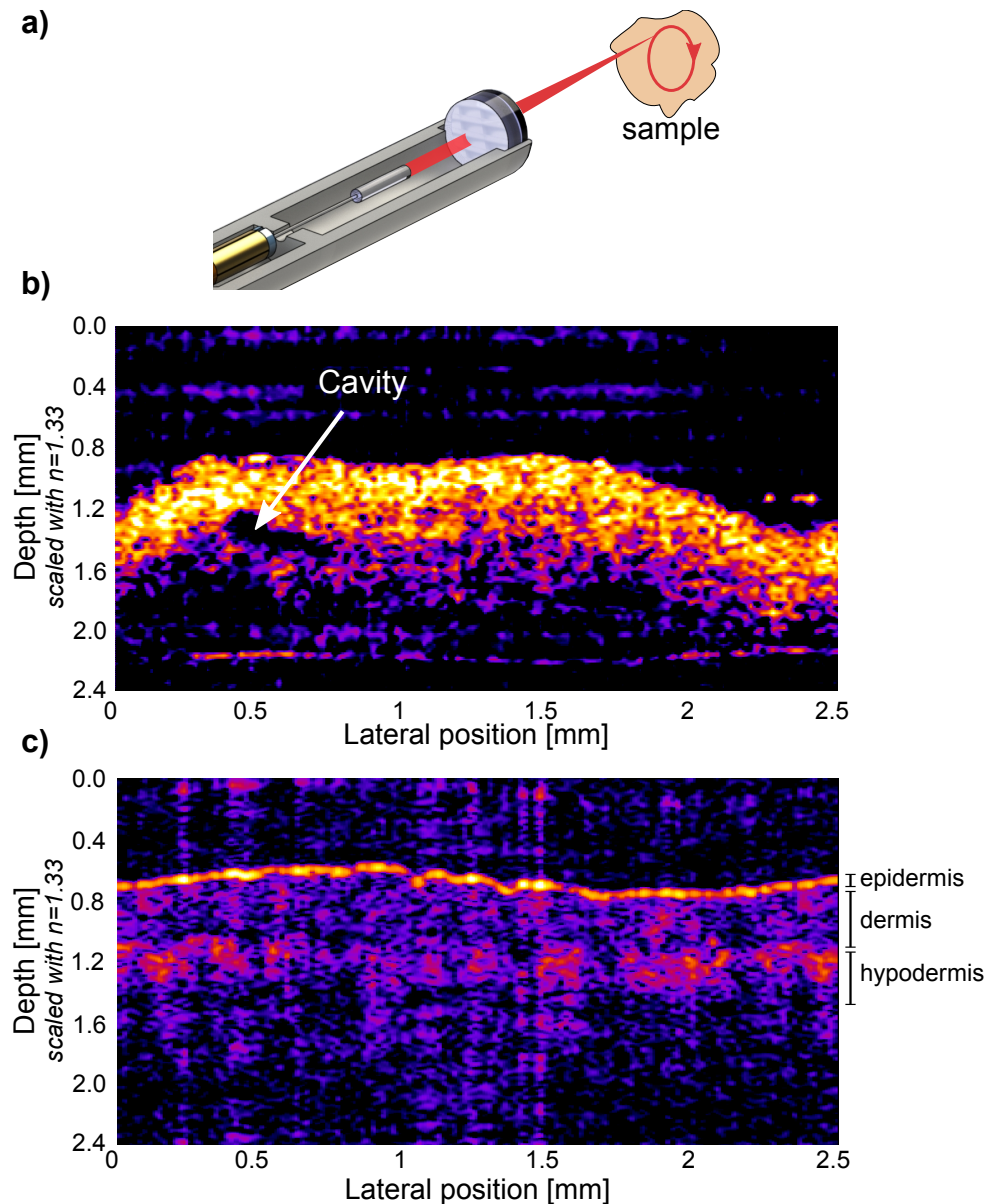


Figure 5.8: a) Illustration of the measurement arrangement for the circular B-Scan used as a proof of concept of OCT. b) Image of a circular OCT B-Scan of a colon polyp with a diameter $d = 0.8 \text{ mm}$. Structural changes within the tissue can be detected and at the current state of the investigation the images suggest that blood vessels can be detected. c) Image of a circular OCT B-Scan of a human finger tip, where the epidermis, dermis and hypodermis can be tentatively differentiated.

5 Experimental Evaluation

6 Conclusion & Outlook

The main goal of this work is the realization of a novel fiber scanner for 3D OCT imaging, designed for its combination with a full field microscope to form a multimodal probe. A tubular piezoelectric fiber scanner is used to perform en face scanning required for 3D OCT measurements. The complete scanning engine has an outer diameter of 0.9 mm and a length of 9 mm, and features custom fabricated 10 μm thick polyimide flexible interconnect lines to address the four piezoelectric electrodes. This scanning engine was tested in a single modality, demonstrator probe with an external diameter of 2.5 mm and a total length of 15 mm, allowing the OCT imaging of a 1 mm field of view with a resolution of 45 μm using 1330 nm light.

To the best of our knowledge, the presented demonstrator probe is also one of the most compact implementation of an OCT microendoscope.

6.1 Conclusion

During this project, the behavior of fiber scanners was analyzed and several approaches were discussed and simulated. It was concluded that its implementation as fourier plane scanner using a GRIN lens as collimator and weight was optimal for OCT. A complete electro-mechano-optical analysis and simulation followed, allowing the optimization of the system to reach diffraction-limited resolution and a maximum field of view.

The size constraints that required the implementation of the scanner in a $1 \times 1 \text{ mm}^2$ channel in the bottom of the bench challenged the electrical contacting of the 800 μm diameter piezoelectric actuator. The solution involved the fabrication of a novel 10 μm thick polyimide ribbon cable that can be rolled around the tube and contacted to it using vias and conductive glue. The cleanroom process proved to be reliable and repeatable, encouraging its use in upcoming projects.

This work also demonstrated the bonding of a single mode, 80 μm optical fiber to a GRIN lens using a custom silicon microfabricated tool. This method allowed a placement accuracy in the μm range, creating an optical and mechanical bond that operates reliably under the high mechanical stress found in a resonant scanner. Prior OCT setups including GRIN lenses showed that they can cause problematic backreflections. This problem was successfully avoided by a custom GRIN lens design with a 1° tilted exit facet. This solution, together with an special attention to the layout of the optical components, resulted in an optical system with backreflections below 0.02%.

6 Conclusion & Outlook

The assembly of the single mode demonstrator was successfully achieved using alignment features integrated in a 3D-printed housing. This part was manufactured using a commercial, low cost stereolithographic resin printer that enabled quick iterations of the design. The manufactured demonstrator allowed the analysis and proof of concept of the fiber scanner concept. Experimental measurements helped refining the assumptions used in the analytical calculation of the resolution of OCT systems. The resultant theoretical description, which closely matches experimental results, will help in the design of future OCT and confocal systems. Although previous work at IMTEK had proven the use of fiber scanners for confocal imaging [13], further analysis was needed to understand and correct for the imaging distortions caused by whirling. The calibration method used in this work, which can operate in real time, reduces the imaging distortions to a minimum and enables the quantitative analysis of the acquired image. This enabled going one step further in cooperation with the Medical University Vienna, where the OCT imaging concept was proven, creating new opportunities for collaboration.

6.2 Outlook

This thesis sucessfully achieved OCT imaging within the demonstrator probe. Thus, the next step is to integrate the scanner in the bimodal probe, as described in [33]. A render of the proposed bimodal probe is shown in Figure 6.1. As the optical system of the demonstrator is designed to emulate that of the bimodal probe, the same optical performance is to be expected.

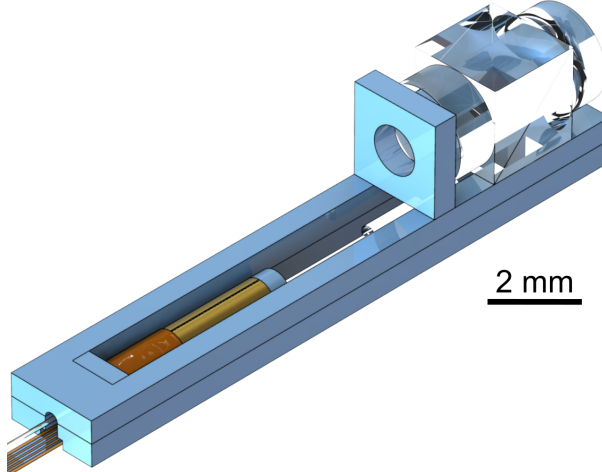


Figure 6.1: CAD image of the proposed bimodal probe, integrating the fiber scanner in the silicon bench. [33]

Bibliography

- [1] K. Fendrich and W. Hoffmann, “More than just aging societies: The demographic change has an impact on actual numbers of patients,” *Journal of Public Health*, vol. 15, no. 5, pp. 345–351, 2007.
- [2] J. M. Jabbour, M. A. Saldua, J. N. Bixler, and K. C. Maitland, “Confocal endomicroscopy: Instrumentation and medical applications,” *Annals of Biomedical Engineering*, vol. 40, no. 2, pp. 378–397, 2012.
- [3] M. S. Bergholt, W. Zheng, K. Lin, K. Y. Ho, M. Teh, K. G. Yeoh, J. B. So, and Z. Huang, “In vivo diagnosis of esophageal cancer using image-guided Raman endoscopy and biomolecular modeling.,” *Technology in cancer research & treatment*, vol. 10, no. 2, pp. 103–12, 2011.
- [4] J. S. Park, Z. Chen, M. Y. Jeong, and C.-S. Kim, “Double common-path interferometer for flexible optical probe of optical coherence tomography,” *Optics Express*, vol. 20, no. 2, p. 1102, 2012.
- [5] J. Sun and H. Xie, “MEMS-based endoscopic optical coherence tomography,” 2011.
- [6] D. Huang, E. A. Swanson, C. P. Lin, J. S. Schuman, W. G. Stinson, W. Chang, M. R. Hee, T. Flotte, K. Gregory, C. A. Puliafito, and J. G. Fujimoto, “Optical Coherence Tomography,” *Science. November*, vol. 22, no. 2545035, pp. 1178–1181, 1991.
- [7] J. A. Flatter and J. Carroll, “Outer Retinal Structure Following Closed Globe Blunt Ocular Trauma,” *Retina*, vol. 55, no. 3, pp. 328–333, 2013.
- [8] F. Feldchtein, G. Gelikonov, V. Gelikonov, R. Kuranov, A. Sergeev, N. Gladkova, A. Shakhov, N. Shakhova, L. Snopova, A. Terent’eva, E. Zaginova, Y. Chumakov, and I. Kuznetzova, “Endoscopic applications of optical coherence tomography.,” *Optics express*, vol. 3, no. 6, pp. 257–270, 1998.
- [9] G. J. Tearney, M. E. Brezinski, B. E. Bouma, S. A. Boppart, C. Pitris, J. F. Southern, and J. G. Fujimoto, “n Vivo Endoscopic Optical Biopsy with Optical Coherence Tomography,” *Science*, vol. 276, no. 1997, pp. 2037–2039, 1997.
- [10] G. J. Tearney, S. A. Boppart, A. E. Bouma, M. E. Brezinski, N. J. Weissman, A. F. Southern, and J. G. Fujimoto, “Scanning single-mode fiber optic catheter-endoscope for optical coherence tomography,” vol. 21, no. 7, 1996.

Bibliography

- [11] T. Xie, D. Mukai, S. Guo, M. Brenner, and Z. Chen, “Fiber-optic-bundle-based optical coherence tomography,” vol. 30, no. 14, pp. 1803–1805, 2005.
- [12] E. J. Seibel, Q. Y. J. Smithwick, C. M. Brown, and P. G. Reinhard, “Single fiber flexible endoscope: general design for small size, high resolution, and wide field of view,” *EOS/SPIE European Biomedical Optics Week*, vol. 4158, no. 2001, pp. 29–39, 2001.
- [13] T. Meinert, *3D-Scanner für konfokale Endomikroskopie*. PhD thesis, IMTEK, 2013.
- [14] L. Huo, J. Xi, Y. Wu, and X. Li, “Forward-viewing resonant fiber-optic scanning endoscope of appropriate scanning speed for 3D OCT imaging.,” *Optics express*, vol. 18, no. 14, pp. 14375–14384, 2010.
- [15] C. M. Lee, C. J. Engelbrecht, T. D. Soper, F. Helmchen, and E. J. Seibel, “Scanning fiber endoscopy with highly flexible, 1 mm catheterscopes for wide-field, full-color imaging,” *Journal of Biophotonics*, vol. 3, no. 5-6, pp. 385–407, 2010.
- [16] L. Liu, L. Wu, J. Sun, E. Lin, and H. Xie, “Miniature endoscopic optical coherence tomography probe employing a two-axis microelectromechanical scanning mirror with through-silicon vias.,” *Journal of biomedical optics*, vol. 16, no. 2, p. 026006, 2011.
- [17] N. Weber, *Highly flexible micro-bench system for endoscopic micro-probes*. PhD thesis, 2012.
- [18] D. Lorensen, B. C. Quirk, M. Auger, W.-J. Madore, R. W. Kirk, N. Godbout, D. D. Sampson, C. Boudoux, and R. a. McLaughlin, “Dual-modality needle probe for combined fluorescence imaging and three-dimensional optical coherence tomography.,” *Optics letters*, vol. 38, no. 3, pp. 266–8, 2013.
- [19] H. Yoo, J. W. Kim, M. Shishkov, E. Namati, T. Morse, R. Shubochkin, J. R. McCarthy, V. Ntziachristos, B. E. Bouma, F. A. Jaffer, and G. J. Tearney, “Intra-arterial catheter for simultaneous microstructural and molecular imaging in vivo.,” *Nature medicine*, vol. 17, no. 12, pp. 1680–4, 2011.
- [20] M. Blattmann, S. Kretschmer, S. Thiele, C. Ataman, H. Zappe, A. Herkommer, and A. Seifert, “Bimodal endoscopic probe combining white-light microscopy and optical coherence tomography,” *Applied Optics*, vol. 55, no. 15, p. 4261, 2016.
- [21] S. Kretschmer, “Entwicklung einer bimodalen mikrooptischen Bank für endoskopische Anwendungen.”
- [22] W. Drexler and J. G. Fujimoto, *Optical Coherence Tomography*. 2008.

Bibliography

- [23] G. D. Boreman and G. D. Boremann, *Modualtion Transfer Function in Optical and Electro-Optical Systems*. 2001.
- [24] A. Arnau and D. Soares, “Fundamentals of piezoelectricity,” *Piezoelectric Transducers and Applications*, pp. 1–38, 2008.
- [25] C. J. Chen, “Electromechanical deflections of piezoelectric tubes with quartered electrodes,”
- [26] Marc J. Madou, *Fundamentals of Microfabrication: The Science of Miniaturization*. CRC Press, 2011.
- [27] H. D. Ford and R. P. Tatam, “Swept-source OCT with coherent imaging fibre bundles,” vol. 7503, no. 0, pp. 18–21, 2009.
- [28] E. J. Seibel, R. S. Johnston, and C. D. Melville, “A full-color scanning fiber endoscope,” *Optical Fibers and Sensors for Medical Diagnostics and Treatment Applications VI*, vol. 6083, pp. 608303–608303–8, 2006.
- [29] S. Moon, S.-W. Lee, M. Rubinstein, B. J. F. Wong, and Z. Chen, “Semi-resonant operation of a fiber-cantilever piezotube scanner for stable optical coherence tomography endoscope imaging.,” *Optics express*, vol. 18, no. 20, pp. 21183–21197, 2010.
- [30] D. Fertis, “Basic Theories and Principles of Nonlinear Beam Deformations, ” ... and Methods to Solve Effectively Complex Nonlinear ..., pp. 1–61, 2006.
- [31] F. J. Rodríguez, D. Ceballos, M. Schüttler, A. Valero, E. Valderrama, T. Stieglitz, and X. Navarro, “Polyimide cuff electrodes for peripheral nerve stimulation,” *Journal of Neuroscience Methods*, vol. 98, no. 2, pp. 105–118, 2000.
- [32] I. L. Yeoh, P. G. Reinhall, M. C. Berg, and E. J. Seibel, “Self-Contained Image Recalibration in a Scanning Fiber Endoscope Using Piezoelectric Sensing,” *Journal of Medical Devices*, vol. 9, no. 1, p. 011004, 2014.
- [33] S. Kretschmer, S. Vilches, M. Blattmann, C. Ataman, and H. Zappe, “Design and optimization of a miniaturized imaging probe for simultaneous endomicroscopy and optical coherence tomography,” p. 100530B, feb 2017.